

Low-energy interactions between doubly charmed baryons and Goldstone bosons from lattice QCD

Jing-Yu Yi^{a,b,d} Ze-Rui Liang^{c,a} Liuming Liu^{d,e,*} De-Liang Yao^{a,b,*}

^a*School of Physics and Electronics, Hunan University, Changsha 410082, China*

^b*Hunan Provincial Key Laboratory of High-Energy Scale Physics and Applications, Hunan University, 410082 Changsha, China*

^c*College of Physics and Hebei Key Laboratory of Photophysics Research and Application, Hebei Normal University, Shijiazhuang, Hebei 050024, China*

^d*Institute of Modern Physics, Chinese Academy of Sciences, Lanzhou 730000, China*

^e*University of Chinese Academy of Sciences, School of Physical Sciences, Beijing 100049, China*

E-mail: yijingyu@hnu.edu.cn, liangzr@hebtu.edu.cn,

liuming@impcas.ac.cn, yaodeliang@hnu.edu.cn

ABSTRACT: We perform a lattice QCD calculation of the S -wave interactions between the ground-state spin-1/2 doubly charmed baryons and Goldstone bosons. The lattice QCD simulations are carried out on four 2 + 1 flavor Wilson-Clover ensembles generated by the CLQCD collaboration, with a lattice spacing $a = 0.07746$ fm and two different pion masses, $M_\pi \sim 210$ and ~ 300 MeV. Energy levels are extracted for four single channels, $\Omega_{cc}\bar{K}^{(-2,1/2)}$, $\Xi_{cc}K^{(1,1)}$, $\Xi_{cc}K^{(1,0)}$, and $\Xi_{cc}\pi^{(0,3/2)}$, where the superscripts (S, I) denote strangeness S and isospin I . Our results indicate that the $\Xi_{cc}K^{(1,0)}$ channel is attractive, exhibiting negative energy shifts relative to the non-interacting two-hadron thresholds, while the other three channels are repulsive. Using Lüscher's finite-volume formula, we extract the near-threshold phase shifts and determine the S -wave scattering lengths. Furthermore, a virtual state pole is found in the $\Xi_{cc}K^{(1,0)}$ scattering amplitude. These results provide *ab initio* input to enable high-precision studies of the properties and spectroscopy of doubly heavy baryons.

*Corresponding author

Contents

1	Introduction	1
2	Lattice setup	3
3	Finite-volume spectra	4
3.1	Interpolating operators	4
3.2	Spectra of the single particles	6
3.3	Finite-volume spectra of the two-hadron systems	7
4	Scattering analysis	10
4.1	Lüscher's formula and effective range expansion	10
4.2	Scattering lengths	11
4.3	Pole analysis of the scattering amplitude	16
5	Summary and outlook	16
A	Extraction of energies	17
B	Influence of coupled-channel effects	24
C	Wick contractions	24

1 Introduction

The study of doubly charmed baryons (DCBs), predicted by the SU(4) version of the traditional quark model [1], plays an essential role not only in completing the charmed hadron spectroscopy [2] but also in probing the non-perturbative dynamics of low-energy quantum chromodynamics (QCD) in the presence of two heavy quarks. These states, consisting of two charm quarks and one light quark, serve as ideal systems for investigating heavy quark symmetry, chiral dynamics, and strong interaction mechanisms that are not easily accessible in singly-heavy or light hadrons; see, e.g., refs. [3–7] for recent reviews.

In the past decade, significant experimental progress has been made in the investigation of DCBs; however, many questions remain open. The first observation of Ξ_{cc}^{++} was reported by the LHCb collaboration [8] in 2017 through the decay mode $\Lambda_c^+ K^- \pi^+ \pi^+$, with a mass of approximately 3621 MeV and a statistical significance exceeding 12σ . Note that the discovery potential of Ξ_{cc}^{++} in the $\Lambda_c^+ K^- \pi^+ \pi^+$ mode was suggested by the theoretical work [9]. This finding was subsequently supported by observations in other decay channels such as $\Xi_{cc}^{++} \rightarrow \Xi_c^{(\prime)+} \pi^+$ [10, 11] and $\Xi_{cc}^{++} \rightarrow \Xi_c^0 \pi^+ \pi^+$ [12]. More precise measurements

followed, yielding improved mass and lifetime estimates [13, 14], as well as production cross-section data in proton-proton collisions at 13 TeV [15]. These results are broadly consistent with predictions from quark models [16, 17], as well as with those from QCD sum rules [18–20] and earlier lattice QCD calculations [21–23]. In contrast, its isospin partner Ξ_{cc}^+ and the strange cousin Ω_{cc}^+ in the same SU(3) triplet have not yet been firmly observed. An earlier claim of Ξ_{cc}^+ observation by the SELEX collaboration [24, 25], with a mass near 3520 MeV, was not corroborated by subsequent experiments such as FOCUS [26], BaBar [27], Belle [28], or LHCb [29, 30]. Moreover, the SELEX mass value is in tension with modern theoretical predictions (e.g., Refs. [31–33]). Recent searches conducted by LHCb for decay signatures of Ξ_{cc}^+ and Ω_{cc}^+ have not yielded significant signals [34, 35], indicating that their production and decay mechanisms are not yet well understood.

Complementary to experimental measurements, lattice QCD provides a first-principle approach to explore the properties of DCBs directly from QCD. Extensive and high-precision calculations of the DCB spectrum have been performed using a variety of lattice formulations [21–23, 36–48], including simulations with $N_f = 2 + 1$ and $N_f = 2 + 1 + 1$ dynamical fermions. These state-of-the-art calculations employ strategies such as computations directly at the physical pion mass [41, 45, 48], as well as those at unphysical pion masses followed by controlled continuum extrapolations, e.g., ref. [46]. The most recent lattice QCD result [48], $M_{\Xi_{cc}} = 3.634(51)$ GeV, is in excellent agreement with the LHCb measurement of Ξ_{cc}^{++} [8] and disfavours the earlier SELEX value [24, 25]. Beyond the mass spectrum, lattice QCD has also been applied to explore a range of other properties, including electromagnetic form factors [49–52], radiative transitions [53], and thermal behavior [54], which provide further insights into the structural and dynamic characteristics of the DCBs.

Despite these advances, a lattice QCD study of the interactions between DCBs and Goldstone bosons is still missing. Nevertheless, previous efforts have been made by imposing baryon chiral perturbation theory (BChPT) [55–57], the effective field theory [58] of QCD at low energies. In ref. [59], the S -wave scattering lengths of the DCBs $B_{cc} \in \{\Xi_{cc}^{++}, \Xi_{cc}^+, \Omega_{cc}^+\}$ and the Goldstone bosons $\phi \in \{\pi^0, \pi^\pm, K^0, K^\pm, \bar{K}^0, \eta\}$ are derived within the heavy baryon (HB) formalism of BChPT. The non-relativistic calculation [59] is upgraded to a relativistic one [60] by using the extended-on-mass-shell (EOMS) renormalization scheme [61], where the S - and P -wave scattering lengths, together with the S -wave phase shifts, are systematically predicted. The chiral amplitudes have been utilized to investigate the dynamically generated exotic DCB baryons in Refs. [62, 63]. By using the $\mathcal{O}(p^2)$ chiral potentials and incorporating the P -wave excitations between the two charm quarks, two quasistable states in the spectrum of negative-parity DCBs are found in ref. [63]. However, the aforementioned BChPT predictions strongly rely on the values of the low-energy constants (LECs), stemming from the $B_{cc}\phi$ chiral Lagrangians [64, 65]. The input LEC values in these works are estimated from the $D\phi$ LECs, determined by fitting to lattice QCD of $D\phi$ interactions in, e.g., refs. [66, 67], via the heavy diquark-antiquark (HDA) symmetry [68], where D stands for ground-state pseudoscalar charmed mesons. Therefore, to obtain precise scattering information on the DCB spectroscopy, it is timely and necessary to carry out a lattice QCD calculation of the $B_{cc}\phi$ interactions.

In this work, we perform the first lattice QCD calculation of the S -wave scattering between the ground state $J^P = (1/2)^+$ DCBs and the Goldstone bosons. We use four $N_f = 2 + 1$ gauge ensembles generated by the CLQCD collaboration [69], with a lattice spacing $a = 0.07746$ fm and two pion masses $M_\pi \sim 210$ and 300 MeV. We focus on four single-channel elastic scattering processes: $\Omega_{cc}\bar{K}^{(-2,1/2)}$, $\Xi_{cc}K^{(1,1)}$, $\Xi_{cc}K^{(1,0)}$, and $\Xi_{cc}\pi^{(0,3/2)}$, which are classified by the superscripts (S, I) with S and I denoting strangeness and isospin, respectively. Pertinent interpolating operators for the DCBs and the Goldstone bosons are constructed, based on which the two-hadron operators that transform under the irreducible representation (irrep) G_1^- of the discrete group $O_h^{(2)}$ are deduced, following the procedure detailed in ref. [70]. For each scattering channel, finite-volume energy levels are extracted from the correlation functions of the corresponding operators. Our results reveal that the $\Xi_{cc}K^{(1,0)}$ channel is attractive at both pion masses, exhibiting downward energy shifts from the free thresholds, while the other three channels are repulsive. The scattering phase shifts are then obtained from the finite-volume energy levels via Lüscher's finite volume method [71, 72]. Consequently, we extract the S -wave scattering lengths and effective ranges, which are defined in the effective range expansion (ERE) parametrization of the threshold amplitude for the four channels. The scattering lengths are extrapolated to the physical point and are found to be consistent with the BChPT predictions [59, 60], justifying the use of HDA symmetry in the estimate of the $B_{cc}\phi$ LEC values [59, 60, 63]. In addition, a virtual state is found in the $\Xi_{cc}K^{(1,0)}$ channel through the pole analysis of the scattering amplitudes.

This manuscript is structured as follows. The lattice setup is briefly introduced in section 2. The finite-volume spectra are presented in 3. Scattering analysis using Lüscher formula is done in section 4, where scattering lengths, effective ranges, and poles are discussed in detail. Our summary and outlook are presented in section 5. Numerical results of the correlation functions are relegated to appendix A. Interpolators and masses needed for the estimate of coupled-channel effects from the singly charmed baryons B_c and charm D mesons are shown in appendix B. Appendix C presents the quark contraction diagrams required for the computation of correlation functions of two-hadron systems.

2 Lattice setup

The results presented in this paper are based on the gauge configurations generated by the CLQCD Collaboration with $2 + 1$ dynamical quark flavors using the tadpole improved tree-level Symanzik gauge action and Clover fermion action [69]. We use four ensembles with the same lattice spacing $a = 0.07746$ fm and two different pion masses $M_\pi \simeq 305$ MeV and $M_\pi \simeq 207$ MeV. Details of the ensembles are listed in Table 1. Among these ensembles, F32P21/F48P21 and F32P30/F48P30 are two couples that share the same pion mass but have different volumes to obtain more kinematic points in the finite-volume spectra, thereby rendering a more robust determination of the scattering parameters. The action of the valence charm quark is the Fermilab action [73], which controls discretization errors of $\mathcal{O}(am_c)^n$. The tuning of the parameters in the Fermilab action follows the method applied in Ref. [23].

ID	β	a (fm)	am_l	am_s	M_π (MeV)	$L^3 \times T$	$N_{\text{cfgs.}}$
F32P30	6.41	0.07746(18)	-0.2295	-0.2050	303.9(0.6)	$32^3 \times 96$	750
F48P30	6.41	0.07746(18)	-0.2295	-0.2050	304.9(0.4)	$48^3 \times 96$	359
F32P21	6.41	0.07746(18)	-0.2320	-0.2050	208.1(1.9)	$32^3 \times 64$	459
F48P21	6.41	0.07746(18)	-0.2320	-0.2050	207.4(0.7)	$48^3 \times 96$	222

Table 1: Details of the four ensembles used in this work, including ensemble identifier (ID), gauge coupling β , lattice spacing a , dimensionless bare quark mass parameters for light and strange quarks (am_l , am_s), pion mass M_π , lattice volume $L^3 \times T$, and number of gauge configurations $N_{\text{cfgs.}}$.

Quark propagators are computed using the distillation quark smearing method [74]. The smearing operator is composed of a small number (N_{ev}) of the eigenvectors associated with the N_{ev} lowest eigenvalues of the three-dimensional Laplacian on the HYP-smeared gauge field. The number of eigenvectors N_{ev} is 100 for all four ensembles. We have verified that increasing N_{ev} to 200 for the large-volume ensembles (F48P30 and F48P21) yields consistent energy levels. The statistical uncertainty is estimated using the bootstrap method with 4000 samples.

3 Finite-volume spectra

In this section, we present the spectra of the relevant single hadrons and two-hadron systems, which will be used to extract the scattering information via Lüscher's method. We begin by detailing the construction of interpolating operators for both single- and two-hadron states, followed by a presentation of their corresponding numerical energy levels.

3.1 Interpolating operators

The single-hadron interpolating operators for the Goldstone bosons, π^+ , K^+ and K^0 , are given by

$$\begin{aligned}\mathcal{O}_{\pi^+}(x) &= \bar{d}(x)_\alpha^a (\gamma_5)_{\alpha\beta} u(x)_\beta^a , \\ \mathcal{O}_{K^+}(x) &= \bar{s}(x)_\alpha^a (\gamma_5)_{\alpha\beta} u(x)_\beta^a , \\ \mathcal{O}_{K^0}(x) &= \bar{s}(x)_\alpha^a (\gamma_5)_{\alpha\beta} d(x)_\beta^a ,\end{aligned}\tag{3.1}$$

where the Greek and Latin letters denote the Dirac and color indices, respectively; and summation over repeated indices is implied. The interpolators for π^- , K^- and \bar{K}^0 can be readily obtained by performing charge conjugation. For the ground states of doubly charmed baryons $\Xi_{cc}^{++,+}$ and Ω_{cc}^+ with $J^P = (1/2)^+$, the interpolators read:

$$\begin{aligned}\mathcal{O}_{\Xi_{cc}^{++}}(x) &= \epsilon^{ijk} P_+ [c^{iT}(x) C \gamma_5 u^j(x)] c^k(x) , \\ \mathcal{O}_{\Xi_{cc}^+}(x) &= \epsilon^{ijk} P_+ [c^{iT}(x) C \gamma_5 d^j(x)] c^k(x) , \\ \mathcal{O}_{\Omega_{cc}^+}(x) &= \epsilon^{ijk} P_+ [c^{iT}(x) C \gamma_5 s^j(x)] c^k(x) ,\end{aligned}\tag{3.2}$$

where $C = i\gamma_2\gamma_0$ is the charge conjugation matrix and the positive parity projector is defined by $P_+ = (1 + \gamma_0)/2$. Only the color indices are shown explicitly, while the Dirac indices are suppressed to adhere to the vector/matrix notation. For a hadron state of definite spatial momentum \mathbf{p} , the corresponding interpolator can be generically expressed as

$$\mathcal{O}_h(\mathbf{p}, t) = \sum_{\mathbf{x}} \mathcal{O}_h(\mathbf{x}, t) e^{i\mathbf{p}\cdot\mathbf{x}} , \quad h \in \{\pi^\pm, K^\pm, K^0, \bar{K}^0, \Xi_{cc}^{++}, \Xi_{cc}^+, \Omega_{cc}^+\} , \quad (3.3)$$

with $\mathcal{O}_h(\mathbf{x}, t) \equiv \mathcal{O}_h(x)$ given by Eq. (3.1) for mesons and Eq. (3.2) for baryons. On the lattice, the momentum takes values of $\mathbf{p} = (n_x, n_y, n_z) \times (2\pi/L)$ with $n_{x,y,z}$ being integers.

It is well acknowledged that the two-hadron states in the continuum can be classified by the irreducible representations of the $SU(2)$ group, which are denoted by the total angular momentum $J = 0, 1/2, 1, \dots$. However, the continuum $SU(2)$ group is reduced to the discrete double covering group $O^{(2)}$ of the cubic group O on the lattice. When parity is taken into account, the $O^{(2)}$ is further promoted to $O_h^{(2)} = O^{(2)} \otimes Z_2$, with $Z_2 = \{E = I^2, I\}$ incorporating the spatial inversion I . Consequently, the construction of two-hadron operators from the one-hadron interpolators in eq. (3.3) should be carried out according to the irrep $\Gamma = \{A_1^\pm, A_2^\pm, E^\pm, T_1^\pm, T_2^\pm, G_1^\pm, G_2^\pm, H^\pm\}$ of the discrete group $O_h^{(2)}$. A variety of approaches, such as the partial-wave [70, 75, 76], projection [70, 77], and helicity methods [70, 78], have been proposed for constructing lattice operators that describe the scattering of particles with arbitrary spin.

Within the projection method, the two-hadron operator that transforms under the irrep Γ of $O_h^{(2)}$ is defined by

$$\mathcal{O}_{p,\Gamma,r}^{h_1 h_2} = \sum_{g \in O_h^{(2)}} T_{rr}^\Gamma(g) g [\mathcal{O}_{h_1}(\mathbf{p}_1) \mathcal{O}_{h_2}(\mathbf{p}_2)] g^{-1} , \quad (3.4)$$

where $T^\Gamma(g)$ stands for the matrix of the irrep Γ . The summation runs over the 96 elements in the $O_h^{(2)} = \{\dots, g, \dots\}$ group. The momenta \mathbf{p}_1 and \mathbf{p}_2 satisfy $\mathbf{p}_1 + \mathbf{p}_2 = 0$ and $|\mathbf{p}_1| = |\mathbf{p}_2| \equiv p$, ensuring that the parity of the two-particle system is a good quantum number. The projection method leads to lattice operators that transform according to a given irrep Γ . In our case, the S -wave $B_{cc}\phi$ system with $J^P = (1/2)^-$ in the continuum corresponds to the irrep G_1^- on the lattice. Due to the reduced symmetry of the lattice, the irrep G_1^- contains mixing from higher angular momenta $J \geq 7/2$, which are sufficiently high to be ignored in our calculations.

Eventually, for a given relative momentum modulus p , the scattering operators with definite (S, I) quantum numbers are constructed as

$$\begin{aligned} \mathcal{O}_p^{\Xi_{cc} K^{(1,0)}} &= \frac{1}{\sqrt{2}} \sum_{\alpha, \mathbf{p}_1, \mathbf{p}_2} C_{\alpha, \mathbf{p}_1, \mathbf{p}_2} \left(\mathcal{O}_{\Xi_{cc}^{++}, \alpha}(\mathbf{p}_1) \mathcal{O}_{K^0}(\mathbf{p}_2) - \mathcal{O}_{\Xi_{cc}^+, \alpha}(\mathbf{p}_1) \mathcal{O}_{K^+}(\mathbf{p}_2) \right) , \\ \mathcal{O}_p^{\Xi_{cc} K^{(1,1)}} &= \sum_{\alpha, \mathbf{p}_1, \mathbf{p}_2} C_{\alpha, \mathbf{p}_1, \mathbf{p}_2} \left(\mathcal{O}_{\Xi_{cc}^{++}, \alpha}(\mathbf{p}_1) \mathcal{O}_{K^+}(\mathbf{p}_2) \right) , \\ \mathcal{O}_p^{\Omega_{cc} \bar{K}^{(-2,1/2)}} &= \sum_{\alpha, \mathbf{p}_1, \mathbf{p}_2} C_{\alpha, \mathbf{p}_1, \mathbf{p}_2} \left(\mathcal{O}_{\Omega_{cc}^+, \alpha}(\mathbf{p}_1) \mathcal{O}_{\bar{K}^0}(\mathbf{p}_2) \right) , \end{aligned}$$

$$\mathcal{O}_p^{\Xi_{cc}\pi^{(0,3/2)}} = \sum_{\alpha, \mathbf{p}_1, \mathbf{p}_2} C_{\alpha, \mathbf{p}_1, \mathbf{p}_2} \left(\mathcal{O}_{\Xi_{cc}^{++}, \alpha}(\mathbf{p}_1) \mathcal{O}_{\pi^+}(\mathbf{p}_2) \right) . \quad (3.5)$$

Here, α is the Dirac index of the doubly charmed baryon field. The coefficients $C_{\alpha, \mathbf{p}_1, \mathbf{p}_2}$ are chosen to ensure the operators transform under the irrep G_1^- . In Table 2, we list the values of $C_{\alpha, \mathbf{p}_1, \mathbf{p}_2}$ for the lowest three momenta $p^2 = 0, 1, 2$ (in units of $(2\pi/L)^2$).

	α	\mathbf{p}_1	\mathbf{p}_2	$C_{\alpha, \mathbf{p}_1, \mathbf{p}_2}$
$p = 0$	1	(0, 0, 0)	(0, 0, 0)	1
	1	(-1, 0, 0)	(1, 0, 0)	1
	1	(1, 0, 0)	(-1, 0, 0)	1
	1	(0, -1, 0)	(0, 1, 0)	1
	1	(0, 1, 0)	(0, -1, 0)	1
	1	(0, 0, -1)	(0, 0, 1)	1
	1	(0, 0, 1)	(0, 0, -1)	1
	1	(-1, -1, 0)	(1, 1, 0)	1
	1	(1, 1, 0)	(-1, -1, 0)	1
	1	(-1, 0, -1)	(1, 0, 1)	1
$p = 1$	1	(1, 0, 1)	(-1, 0, -1)	1
	1	(0, -1, -1)	(0, 1, 1)	1
	1	(0, 1, 1)	(0, -1, -1)	1
	1	(-1, 1, 0)	(1, -1, 0)	1
	1	(1, -1, 0)	(-1, 1, 0)	1
	1	(-1, 0, 1)	(1, 0, -1)	1
	1	(1, 0, -1)	(-1, 0, 1)	1
	1	(0, 1, -1)	(0, -1, 1)	1
	1	(0, -1, 1)	(0, 1, -1)	1
$p = \sqrt{2}$	1	(1, 1, 1)	(-1, -1, -1)	1
	1	(-1, -1, 1)	(1, 1, -1)	1
	1	(1, -1, -1)	(-1, 1, 1)	1
	1	(-1, 1, -1)	(1, -1, 1)	1
	1	(1, 0, 1)	(-1, 0, -1)	1
	1	(0, 1, -1)	(1, 0, 1)	1
	1	(0, -1, 1)	(-1, 0, 1)	1
	1	(1, 0, -1)	(-1, 0, 1)	1
	1	(0, 1, 1)	(0, -1, 1)	1
	1	(0, -1, -1)	(0, 1, -1)	1

Table 2: Values of the coefficients $C_{\alpha, \mathbf{p}_1, \mathbf{p}_2}$ in the two-particle operators (3.5) for the momenta $p^2 = 0, 1, 2$, in units of $(2\pi/L)^2$.

3.2 Spectra of the single particles

The masses of the single particles are obtained from the correlation functions of the respective interpolating operators defined in eq. (3.3):

$$C_h(\mathbf{p}, t) = \sum_{t_{\text{src}}} \langle \mathcal{O}_h(\mathbf{p}, t + t_{\text{src}}) \mathcal{O}_h^\dagger(\mathbf{p}, t_{\text{src}}) \rangle . \quad (3.6)$$

The source time t_{src} is summed over all time slices to enhance the statistics. The dispersion relation $E^2 = m_0^2 + c^2 \mathbf{p}^2$ is investigated by calculating the single-particle energies at the five lowest momenta on lattice: $\mathbf{p} = (0, 0, 0), (0, 0, 1), (0, 1, 1), (1, 1, 1), (0, 0, 2)$ in units of $\frac{2\pi}{L}$. The effective masses for pion, kaon, Ξ_{cc} and Ω_{cc} at the five momenta are displayed in figures 4 to 7 of section A, respectively. We fit the correlation functions to an exponential form $C(t) = A e^{-Et}$ for the baryons and a cosh function $C(t) = A \cosh[E(T - \frac{t}{2})]$ for the

mesons to obtain the energies. The masses of the single particles at zero momentum are listed in table 3. The results of dispersion relation fits are given in table 4. The fitted parameter c^2 deviates slightly from unity due to lattice artifacts, but its proximity to one indicates that these effects are small. The rest masses m_0 extracted from the dispersion relation fits are in perfect agreement with those from direct correlator fits (c.f. table 3).

	π	K	Ξ_{cc}	Ω_{cc}
F32P30	303.9(6)	523.0(4)	3632.4(9)	3713.7(6)
F48P30	304.9(4)	524.1(3)	3637.2(1.3)	3717.9(1.0)
F32P21	208.1(1.9)	491.7(7)	3605.6(1.4)	3693.8(8)
F48P21	207.4(7)	491.1(3)	3607.6(1.8)	3699.7(1.0)

Table 3: Masses of single particles, in units of MeV.

Particle	Ensemble	m_0 (MeV)	c^2	χ^2/dof
π	F32P30	303.96(60)	1.0069(42)	0.69
	F48P30	304.87(39)	1.0075(22)	1.02
	F32P21	208.50(1.90)	1.0582(94)	0.73
	F48P21	207.74(69)	1.0157(37)	1.58
K	F32P30	523.00(43)	1.0026(23)	1.47
	F48P30	524.07(28)	1.0034(15)	0.53
	F32P21	491.73(69)	1.0097(52)	0.26
	F48P21	491.09(33)	1.0081(25)	0.63
Ξ_{cc}	F32P30	3633.0(8)	0.9915(61)	1.70
	F48P30	3636.9(1.2)	0.9640(190)	0.38
	F32P21	3605.5(1.4)	1.0060(100)	0.48
	F48P21	3608.0(1.6)	1.0520(220)	0.56
Ω_{cc}	F32P30	3713.9(6)	0.9747(37)	0.92
	F48P30	3717.9(1.0)	0.9670(200)	0.44
	F32P21	3693.8(8)	0.9801(51)	0.11
	F48P21	3699.5(1.0)	0.9980(130)	1.16

Table 4: Results of single-particle masses m_0 and dispersion-relation coefficients c^2 , obtained by fitting the single particle energies at the five lowest momenta to the dispersion relation $E^2 = m_0^2 + c^2 \mathbf{p}^2$.

3.3 Finite-volume spectra of the two-hadron systems

The energies of the scattering systems can be extracted from the correlation functions of the two-hadron operators. For each channel under consideration, a correlation matrix is

constructed as

$$\mathbf{C}_{ij}(t) = \sum_{t_{\text{src}}} \left\langle \mathcal{O}_i(t + t_{\text{src}}) \mathcal{O}_j^\dagger(t_{\text{src}}) \right\rangle, \quad (3.7)$$

where \mathcal{O}_i and \mathcal{O}_j are given in eq. (3.5), and the subscripts i, j label different values of momenta p . In the case that $p = \{0, 1, \sqrt{2}\}(2\pi/L)$, the correlation function is a 3×3 matrix. The quark contraction diagrams for the four channels, $\Omega_{cc}\bar{K}^{(-2,1/2)}$, $\Xi_{cc}K^{(1,1)}$, $\Xi_{cc}K^{(1,0)}$ and $\Xi_{cc}\pi^{(0,3/2)}$, required in our simulation, are shown in figures 12 to 15 of section C, respectively.

The finite-volume energy spectra of two-hadron systems can be determined through a systematic analysis of the correlation function matrices \mathbf{C} using the variational technique suggested in ref. [79]. Specifically, the generalized eigenvalue problem (GEVP) [79, 80] is solved with a fixed time slice t_0 . In this study, we choose $t_0 = 3$ in lattice units and have verified that the resulting energies are stable against variations of this choice:

$$\mathbf{C}(t)v^{(n)}(t) = \lambda_n(t)\mathbf{C}(t_0)v^{(n)}(t), \quad n = 1, 2, 3, \quad (3.8)$$

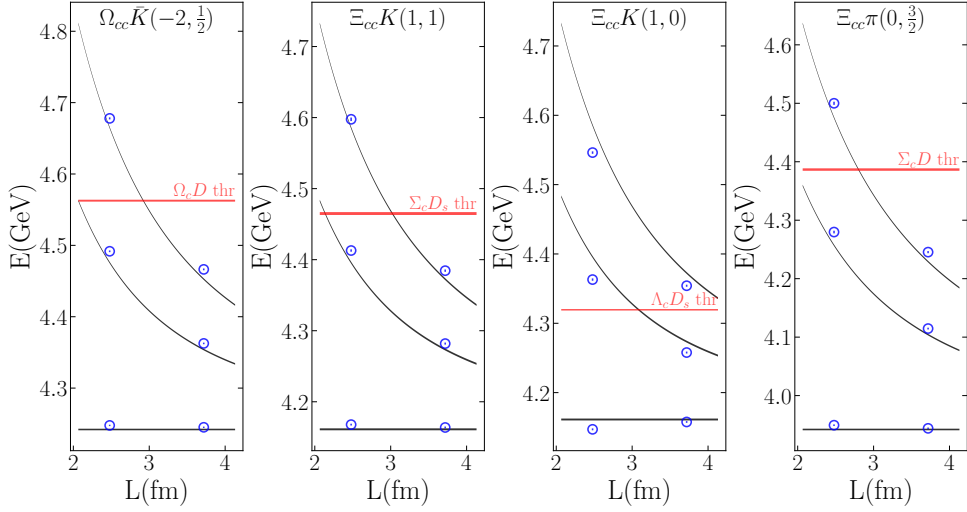
where λ_n and $v^{(n)}$ denote eigenvalues and eigenvectors, respectively. The energies E_n are extracted from the eigenvalues $\lambda_n(t)$ by

$$\lambda_n(t) = (1 - A_n)e^{-E_n(t-t_0)} + A_n e^{-E'_n(t-t_0)}, \quad (3.9)$$

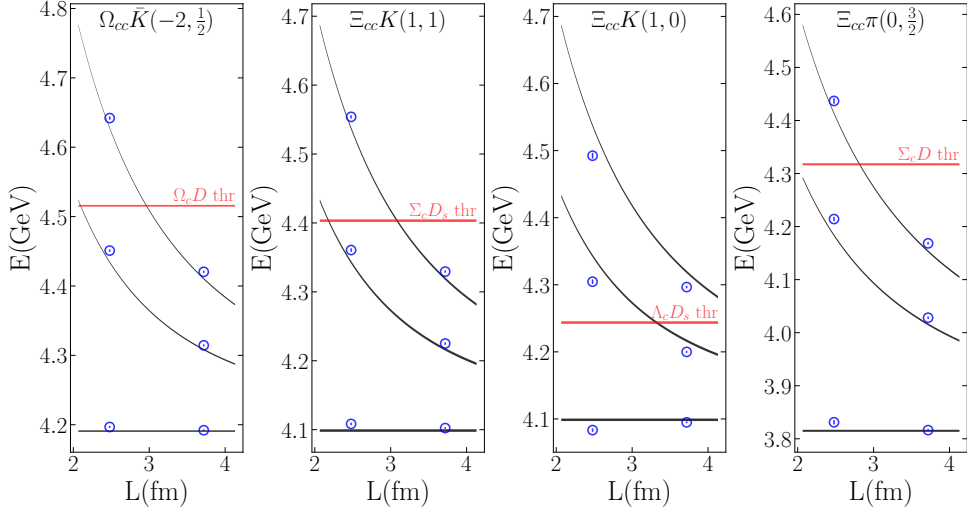
where A_n , E_n , and E'_n are free parameters. E'_n accounts for high-lying energy levels not covered by GEVP analysis. Note that $\lambda_n \rightarrow 1$ as $t \rightarrow t_0$, and the first term dominates for large t since $E'_n > E_n$. We extract the energy levels by performing two-exponential fits to the temporal dependence of the eigenvalues $\lambda_n(t)$ using eq. (3.9). To visualize the fit quality and validate our choice of fit ranges, we present plots of the rescaled eigenvalues for the four two-hadron systems in figures 8 to 11 of section A.

Figure 1 shows the obtained energy levels represented by blue points alongside the non-interacting thresholds depicted as black bands for comparison. The $\Xi_{cc}K^{(1,0)}$ channel displays consistent negative energy shifts across both pion mass ensembles; namely, finite-volume energy levels reside below the non-interacting thresholds. This implies that the $\Xi_{cc}K^{(1,0)}$ system is attractive and may form a bound state or virtual state in the infinite-volume limit, necessitating the scattering analysis detailed in section 4. In contrast, the energy levels of the other three channels are slightly above the respective thresholds, which is indicative of repulsive interactions.

Before ending this section, it should be noted that the above single-channel description is strictly valid only for the systems composed of B_{cc} ($cc\bar{q}$) and Goldstone bosons ϕ ($q\bar{q}$). In fact, the two-hadron systems $B_{cc}\phi$ can also couple to channels comprising a singly charmed baryon B_c (cqq) and a charmed meson D ($c\bar{q}$), since the total quark content $ccqq\bar{q}$ remains conserved. For instance, the $\Omega_{cc}\bar{K}^{(-2,1/2)}$ mixes with $\Omega_c D^{(-2,1/2)}$, etc. In figure 1, we plot the relevant $B_c D$ thresholds to transparently assess the influence of the $B_c D$ channels on our energy levels obtained under the single-channel approximation. The required interpolators for $B_c \in \{\Sigma_c^{++}, \Lambda_c^+, \Omega_c^0\}$ and $D \in \{D^0, D_s^+\}$ are constructed and shown in eq. (B.1). Their



(a)



(b)

Figure 1: Energy levels of two-hadron systems for the four single channels. (a) $M_\pi \sim 300$ MeV; (b) $M_\pi \sim 210$ MeV. The blue data points are the finite-volume energies, and the black bands indicate free energies of the non-interacting threshold with different momenta.

masses at unphysical pion masses, ~ 210 and 300 MeV, are estimated using gauge ensembles F48P30 and F48P21, with the results compiled in table 7 in section B. The energy levels above the B_cD thresholds are excluded from our subsequent scattering analysis in section 4, where the contributions of B_cD channels cannot be ignored.

4 Scattering analysis

4.1 Lüscher's formula and effective range expansion

The discrete energy levels of the interacting $B_{cc}\phi$ system, as established in the preceding section, can be expressed as

$$E_p = \sqrt{m_{B_{cc}}^2 + p^2} + \sqrt{m_\phi^2 + p^2} , \quad (4.1)$$

where p is no longer constrained to the original relative momentum mode $n \frac{2\pi}{L}$ ($n = |\mathbf{n}|$ and $\mathbf{n} \in \mathbb{Z}^3$) in the non-interacting case. The shift of p from its free mode encodes the underlying scattering information of the finite-volume $B_{cc}\phi$ spectrum on the lattice, which can be translated to infinite-volume matrix elements by means of the Lüscher's formula [71, 72] and its generalizations [81].

The Lüscher quantization condition relates the finite-volume energy spectra, modified by interactions, to the infinite-volume scattering amplitudes. For a general multi-channel system, the quantization condition in the CM frame reads

$$\det[\mathbf{1} + i\boldsymbol{\Sigma} \cdot \mathbf{T} \cdot (1 + i\mathbf{M})] = 0 , \quad (4.2)$$

where \mathbf{T} is the infinite-volume T-matrix and \mathbf{M} is a matrix of known functions of the dimensionless scattering momentum $q_i = p_i L / 2\pi$ with i being the channel index. For S -wave interaction \mathbf{M} is diagonal. Furthermore, $\boldsymbol{\Sigma} = \text{diag}\{\dots, \rho_i, \dots\}$ is a diagonal matrix with the phase-space factors $\rho_i = 2p_i / \sqrt{s}$ as elements.

In our single-channel case, the S -wave scattering amplitude can be parameterized as

$$T = \frac{1}{p \cot \delta_0 - ip} , \quad (4.3)$$

where δ_0 denotes the S -wave phase shift. Note that we employ a normalization such that the S -matrix element is associated with the T matrix by $S = 1 + 2ipT$ and the unitarity relation reads $\text{Im } T = p|T|^2$. Furthermore, with this normalization, T is identical to the amplitude f_{0+} specified by eq. (2.26) of ref. [60], i.e., $T = f_{0+}$. Consequently, the quantization condition of eq. (4.2) reduces to the well-known form

$$p \cot \delta_0(p) = \frac{2}{L\sqrt{\pi}} \mathcal{Z}_{00}(1; q^2) , \quad q = \frac{pL}{2\pi} , \quad (4.4)$$

where the Lüscher Zeta function is defined by [71]

$$\mathcal{Z}_{00}(s; q^2) = \frac{1}{\sqrt{4\pi}} \sum_{\mathbf{n} \in \mathbb{Z}^3} \frac{1}{(|\mathbf{n}|^2 - q^2)^s} . \quad (4.5)$$

Since p is obtainable from the interacting energy levels via eq. (4.1), one may readily obtain the phase shift $\delta_0(p)$ using eq. (4.4).

At low energies, the scattering amplitude (4.3) can be expanded as a series of p^2 , accompanied by threshold parameters, which is referred to as the ERE. Traditionally, the ERE of the inverse of the scattering amplitude at threshold reads

$$\text{Re} \left(\frac{1}{T} \right) = p \cot \delta_0 = \frac{1}{a_0} + \frac{1}{2} r_0 p^2 + \sum_{n=2}^{\infty} v_n p^{2n} , \quad (4.6)$$

where the threshold parameters a_0 , r_0 and v_n ($n \geq 2$) are referred to as the scattering length, effective range and shape parameters, in order. In the next subsection, we are going to determine the scattering lengths of the four single channels with the help of eqs. (4.4) and (4.6).

4.2 Scattering lengths

By virtue of the Lüscher formula (4.4), the values of $p \cot \delta_0$ at various momenta p can be determined from the interacting energy levels obtained in section 3.3. There are two points to be discussed before extracting $p \cot \delta_0$. The first one is that we shift the finite-volume energy levels according to

$$E_p \rightarrow E_p + [E_\phi^{\text{cont.}}(p) + E_{B_{cc}}^{\text{cont.}}(p)] - [E_\phi^{\text{latt.}}(p) + E_{B_{cc}}^{\text{latt.}}(p)] , \quad (4.7)$$

where $E_h^{\text{cont.}}(p)$ ($h \in \{\phi, B_{cc}\}$) are the energies calculated from the continuum dispersion relation $E_h^{\text{cont.}}(p) = \sqrt{m_h^2 + p^2}$, while $E_h^{\text{latt.}}(p)$ corresponds to the single-particle energies computed on the lattice. Such a shift is implemented to alleviate the lattice artifacts arising from discretization effects following [82–85]. The other point concerns the selection of the energy levels. That is, only the energy levels below the $B_c D$ thresholds are kept in our scattering analysis, as already explained at the end of section 3.3. Our final results of $p \cot \delta_0$, derived from energy levels with the dispersion relation correction (DRC) implemented via eq. (4.7), are shown as red squares and blue dots in figure 2.

We are now in the position to extract the S -wave scattering parameters. To properly account for the statistical correlations between the energy levels, we perform a correlated fit by minimizing a χ^2 function defined at the level of squared momenta,

$$\chi^2(a_0, r_0, \dots) = \sum_{i,j} [p^2(E_i) - p_{\text{ERE}}^2(i, a_0, r_0, \dots)] (C_{\text{cov}}^{-1})_{ij} [p^2(E_j) - p_{\text{ERE}}^2(j, a_0, r_0, \dots)] . \quad (4.8)$$

Here, the indices i, j run over all energy levels included in the fit for a given scattering channel and pion mass. The quantity $p^2(E_i)$ is the squared momentum determined from the i -th lattice energy level E_i by numerically solving eq. (4.1), $p_{\text{ERE}}^2(i, a_0, r_0, \dots)$ is the solution of the the Lüscher quantization condition (4.4) with ERE parametrization (4.6), and C_{cov} is the covariance matrix of the squared momenta.

By truncating the ERE at $\mathcal{O}(p^2)$ (denoted as leading order (LO) hereafter), we obtain the scattering length a_0 and effective range r_0 . The resulting values of a_0 and r_0 are collected in table 5. The labels “Raw” and “DRC” in the table denote the $p \cot \delta_0$ datasets derived from energy levels without and with DRC, respectively. It can be found that the impact of DRC on scattering lengths a_0 is negligible, since it is predominantly determined by the lowest-lying two-particle energy levels nearest to the non-interacting threshold. Those lowest energy levels have zero momentum $p = |\mathbf{p}_{1,2}| = 0$, and the DRC term $c^2 p^2$ in the dispersion relation vanishes. In contrast, the effective range r_0 exhibits pronounced sensitivity to DRC across nearly all scattering channels. For instance, in the $\Xi_{cc}\pi^{(0, \frac{3}{2})}$ system at $M_\pi \sim 300$ MeV, the DRC shifts r_0 from $-0.23(11)$ fm to $-0.03(19)$ fm with χ^2/dof improved from 4.29 to 1.54. We adopt the values from fits to the DRC-applied data

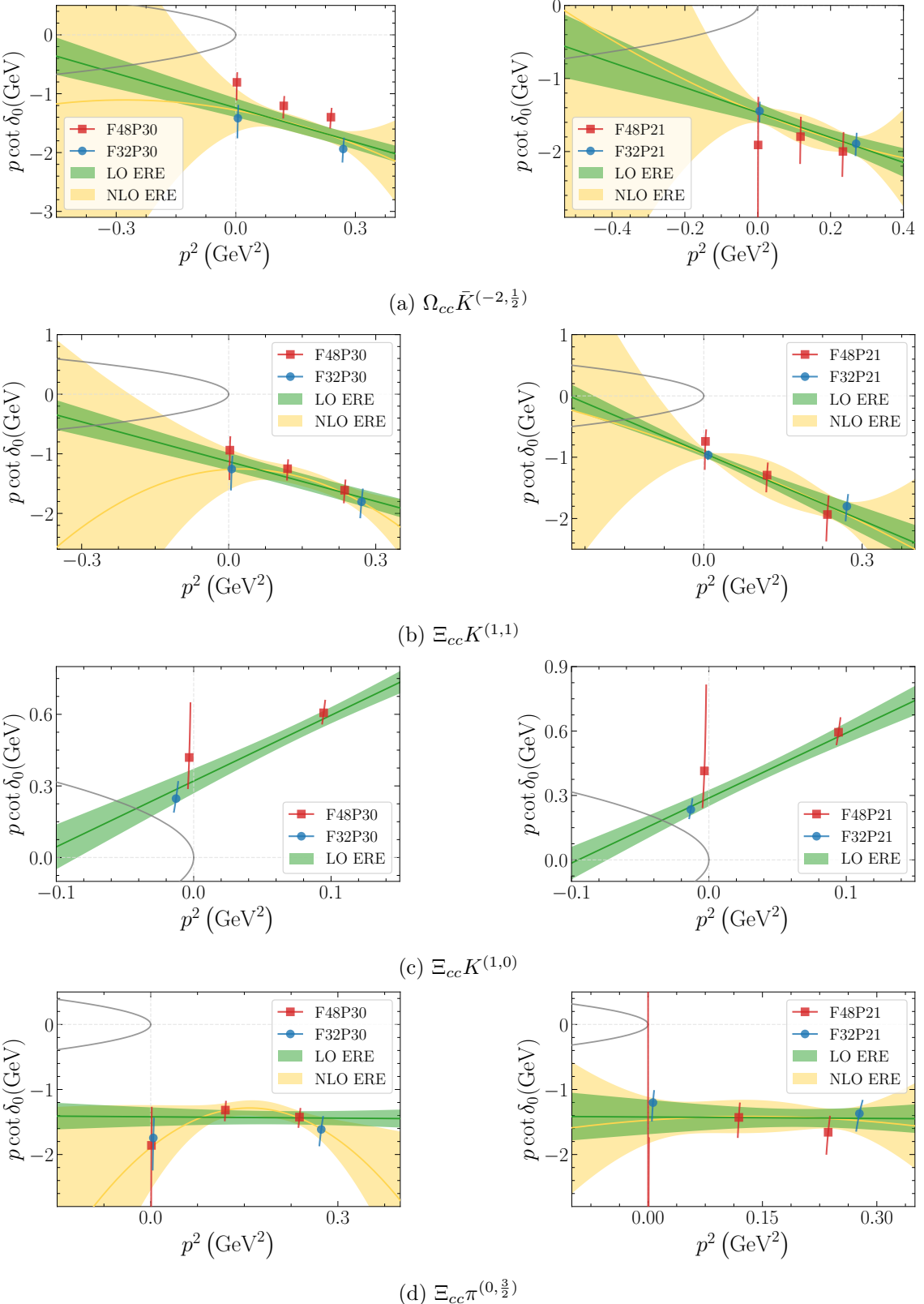


Figure 2: ERE fit results truncated at $\mathcal{O}(p^2)$ (green bands) and $\mathcal{O}(p^4)$ (yellow bands) for four single channels using DRC energy levels. The left and right panels correspond to pion masses $M_\pi \sim 300$ MeV and 210 MeV, respectively. The red and blue points show $p \cot \delta_0$ extracted via Lüscher's formula (eq. (4.2)), while the grey solid curve is $ip = \pm |p|$ versus p^2 .

as our final results for both threshold parameters, although a_0 is robust against the DRC. Based on the fitted values, our LO ERE predictions of $p \cot \delta_0$ are presented as solid green lines with bands in figure 2.

(S, I)	Processes	M_π (MeV)	Data type	a_0 (fm)	r_0 (fm)	χ^2/dof
$(-2, \frac{1}{2})$	$\Omega_{cc}\bar{K} \rightarrow \Omega_{cc}\bar{K}$	300	Raw	-0.172(13)	-1.04(10)	1.11
			DRC	-0.162(20)	-0.77(17)	1.15
		210	Raw	-0.130(11)	-0.40(19)	0.67
			DRC	-0.136(12)	-0.67(25)	0.15
$(1, 1)$	$\Xi_{cc}K \rightarrow \Xi_{cc}K$	300	Raw	-0.184(16)	-1.09(12)	0.30
			DRC	-0.177(22)	-0.88(16)	0.48
		210	Raw	-0.211(14)	-0.88(14)	0.45
			DRC	-0.212(14)	-1.44(29)	0.53
$(1, 0)$	$\Xi_{cc}K \rightarrow \Xi_{cc}K$	300	Raw	0.640(100)	0.98(14)	1.08
			DRC	0.630(100)	1.09(19)	1.05
		210	Raw	0.690(90)	1.29(10)	0.67
			DRC	0.697(90)	1.19(20)	0.69
$(0, \frac{3}{2})$	$\Xi_{cc}\pi \rightarrow \Xi_{cc}\pi$	300	Raw	-0.166(11)	-0.23(11)	4.29
			DRC	-0.140(14)	-0.03(19)	1.54
		210	Raw	-0.149(21)	0.52(28)	1.17
			DRC	-0.143(24)	-0.03(45)	1.02

Table 5: Single-channel S -wave scattering parameters (a_0 , r_0), and the corresponding χ^2/dof obtained from LO ERE fits for four distinct scattering systems at pion masses $M_\pi \sim 300$ MeV and 210 MeV. The raw (uncorrected) and DRC results are compared to quantify deviations in the relativistic dispersion relation of heavy baryons within Lüscher's finite-volume framework.

To assess the influence of the ERE truncation on the scattering lengths, we perform additional fits by employing the ERE expression up to $\mathcal{O}(p^4)$ (labeled as next-to-leading order (NLO) hereafter). Our NLO ERE predictions are shown as yellow lines with bands in figure 2. Due to limited data points and one additional free parameter v_2 , the NLO fits lead to substantially larger uncertainties compared to the LO fits, as can be seen in the figure. In table 6, we compare the results of the scattering length a_0 obtained from the LO and NLO fits. One finds that the scattering length a_0 remains stable under different ERE truncation orders, with deviation within 1σ for most channels. This truncation insensitivity of a_0 aligns with its dominant contribution from near-threshold energy levels. We do not show the effective range r_0 and shape parameter v_2 in table 6 due to their large statistical errors. Note also that the dataset for the $\Xi_{cc}K^{(1,0)}$ channel is insufficient for us to conduct an NLO ERE fit with three free parameters.

In the above, the S -wave scattering lengths for the four distinct channels have been determined at two unphysical pion masses, ~ 300 and 210 MeV. To extrapolate them to the physical pion mass $M_\pi^{\text{phy}} = 135$ MeV, we employ a rank-one polynomial in M_π^2 as

(S, I)	Processes	M_π (MeV)	Data type	a_0 (LO)	a_0 (NLO)	Difference
$(-2, \frac{1}{2})$	$\Omega_{cc}\bar{K} \rightarrow \Omega_{cc}\bar{K}$	300	Raw	-0.172(13)	-0.164(23)	$< 1\sigma$
			DRC	-0.162(20)	-0.159(25)	$< 1\sigma$
		210	Raw	-0.130(11)	-0.135(13)	$< 1\sigma$
			DRC	-0.136(12)	-0.136(13)	$< 1\sigma$
$(1, 1)$	$\Xi_{cc}K \rightarrow \Xi_{cc}K$	300	Raw	-0.184(16)	-0.170(28)	$< 1\sigma$
			DRC	-0.177(22)	-0.163(29)	$< 1\sigma$
		210	Raw	-0.211(14)	-0.212(15)	$< 1\sigma$
			DRC	-0.212(14)	-0.211(20)	$< 1\sigma$
$(0, \frac{3}{2})$	$\Xi_{cc}\pi \rightarrow \Xi_{cc}\pi$	300	Raw	-0.166(11)	-0.111(24)	2.1σ
			DRC	-0.140(14)	-0.110(22)	1.1σ
		210	Raw	-0.149(21)	-0.137(26)	$< 1\sigma$
			DRC	-0.143(24)	-0.140(27)	$< 1\sigma$

Table 6: Comparison of the scattering lengths a_0 determined from LO and NLO ERE fits, with differences quantified in standard deviations (σ).

follows:

$$a_0(M_\pi^2) = \alpha_0 + \alpha_1 M_\pi^2 . \quad (4.9)$$

A more comprehensive extrapolation using the chiral expression from ref. [60] is only feasible once more data points are available from lattice simulations at different pion masses in the future. In figure 3, the blue points represent lattice results at two simulated pion masses, while the blue line and band represent the linear extrapolation with its 1σ statistical uncertainty. For comparison, the ChPT results obtained within the EOMS scheme [60] and HB formalism [59] are displayed as well.

Our final predictions of scattering lengths at the physical pion mass, with statistical and two systematic uncertainties listed sequentially, are:

$$a_0^{\text{phy}}(\Xi_{cc}K^{(1,1)}) = -0.230(24)_{\text{sta}}(5)_{\text{sys}_1}(6)_{\text{sys}_2} \text{ fm} = -0.230(25) \text{ fm} , \quad (4.10)$$

$$a_0^{\text{phy}}(\Xi_{cc}K^{(1,0)}) = 0.730(146)_{\text{sta}}(13)_{\text{sys}_1} \text{ fm} = 0.730(147) \text{ fm} , \quad (4.11)$$

$$a_0^{\text{phy}}(\Xi_{cc}\pi^{(0,3/2)}) = -0.144(37)_{\text{sta}}(3)_{\text{sys}_1}(11)_{\text{sys}_2} \text{ fm} = -0.144(39) \text{ fm} , \quad (4.12)$$

$$a_0^{\text{phy}}(\Omega_{cc}\bar{K}^{(-2,1/2)}) = -0.123(21)_{\text{sta}}(14)_{\text{sys}_1}(2)_{\text{sys}_2} \text{ fm} = -0.123(25) \text{ fm} . \quad (4.13)$$

The central values of the extrapolated results are obtained by performing the linear fit (4.9) to the scattering lengths from the LO ERE analysis with DRC applied. The first uncertainty quoted is the statistical error (sta) propagated from the 1σ uncertainties of the fit parameters. We estimate two dominant sources of systematic uncertainty, both originating from the choice of input values for the extrapolation. The first systematic uncertainty (sys_1) is associated with the DRC, which we quantify as the difference between the central extrapolated value and that obtained using the Raw dataset. The second systematic uncertainty (sys_2) stems from the truncation of the ERE, estimated as the difference when using

the results from the NLO fits as input for the extrapolation. Note that for the $\Xi_{cc}K^{(1,0)}$ channel, the systematic uncertainty from the ERE truncation is not quoted, as an NLO fit was not feasible due to the limited number of data points.

Overall, our results are in good agreement with ChPT predictions at the physical point. Specifically, the scattering lengths of the $\Xi_{cc}K^{(1,0)}$ and $\Xi_{cc}\pi^{(0,\frac{3}{2})}$ channels are consistent with both the EOMS and HB determinations within 1.5σ . In addition, our results favor the EOMS predictions in the $\Omega_{cc}\bar{K}^{(-2,\frac{1}{2})}$ channel but align more closely with the HB predictions in the $\Xi_{cc}K^{(1,1)}$ channel. A crucial caveat for these ChPT predictions is that they rely on the LECs, whose values are estimated from $D\phi$ interactions via HDA symmetry. Note also that for the channels with large scattering lengths, it is actually necessary to refine the chiral amplitudes by performing unitarization, as done in refs. [62, 63].

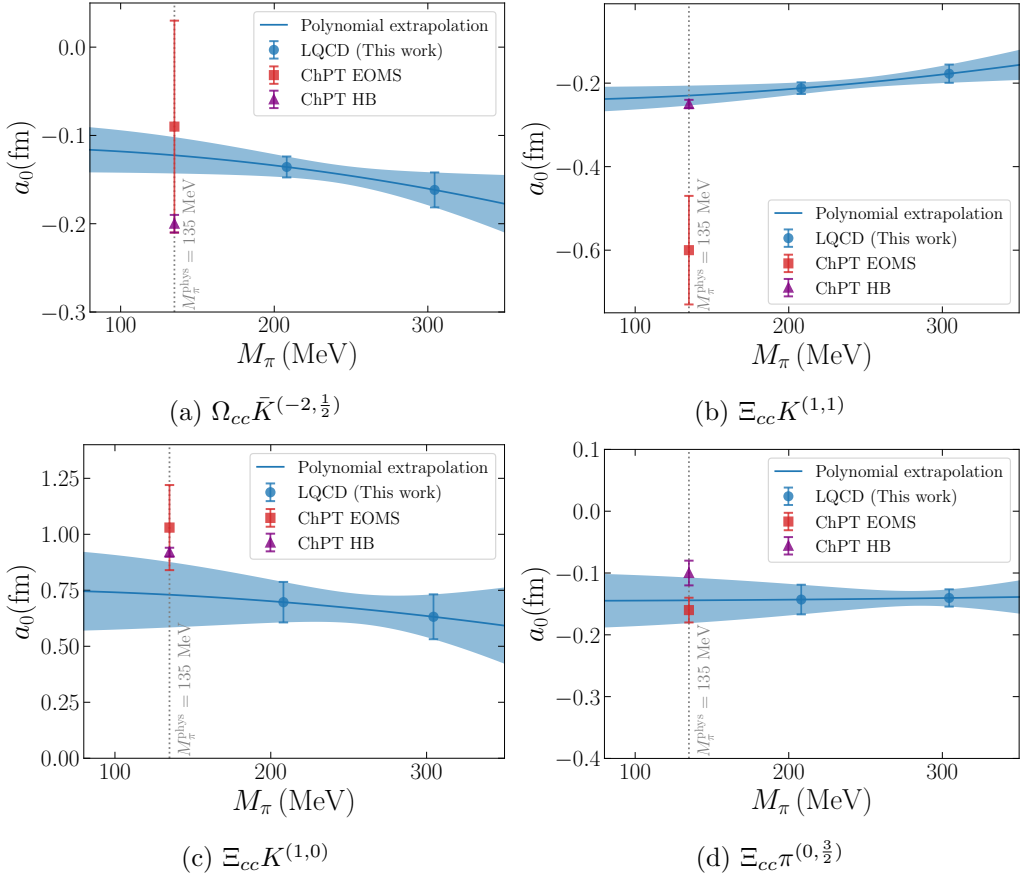


Figure 3: Extrapolation of the S -wave scattering lengths a_0 to the physical pion mass. The results of a_0 labeled by “DRC” from table 5 are adopted in the extrapolation. The EOMS- and HB-ChPT predictions, taken from refs. [59, 60] respectively, are also shown for easy comparison.

4.3 Pole analysis of the scattering amplitude

In S -matrix theory, poles of the elastic scattering amplitude on the real axis of the s -plane below the threshold are identified as bound states (the first Riemann sheet, $\text{Im } p > 0$) or virtual states (the second Riemann sheet, $\text{Im } p < 0$). Equivalently, in the p -plane, bound and virtual states reside on the positive and negative imaginary axes, respectively, which can be readily inferred from $p = \sqrt{(s - s_+)(s - s_-)}/(2\sqrt{s})$ with $s_{\pm} = (M_{B_{cc}} \pm M_{\phi})^2$. Therefore, in view of eq. (4.3), an efficient way to locate these poles is to identify the intersections between the $p \cot \delta_0$ and $ip = \pm|p|$ curves in the range of $p^2 < 0$. To that end, we plot $ip = \pm|p|$ in addition to $p \cot \delta_0$ in figure 2, which are represented by the gray curves. The intersections in the upper and lower half-plane correspond to virtual and bound states, respectively.

Interestingly, the $\Omega_{cc}\bar{K}^{(-2,\frac{1}{2})}$ and $\Xi_{cc}K^{(1,1)}$ channels, previously regarded as repulsive due to upward energy shifts in section 3.3, exhibit bound-state poles in LO ERE fits. The appearance of these unexpected poles is attributed to the LO-truncated ERE and sparse data. On the one hand, the pole positions shift significantly or disappear entirely in the NLO fits, as can be seen from the divergent yellow uncertainty bands in figure 2, demonstrating the instability of the LO results. On the other hand, the poles are located in the range $p^2 < -0.20 \text{ GeV}^2$, which is far beyond the region sampled by our finite-volume energy levels. The resultant existence of those poles is unreliable due to the lack of data to constrain the scattering amplitude in the $p^2 < -0.20 \text{ GeV}^2$ range. Therefore, we refrain from interpreting those poles as any possible physical states in reality. The $\Xi_{cc}\pi^{(0,\frac{3}{2})}$ channel is repulsive, and no poles are found, as can be seen from figure 2d.

The interaction in the $\Xi_{cc}K^{(1,0)}$ channel is attractive, manifesting as negative energy shifts in figure 1. A near-threshold pole at $p^2 \approx -0.03 \text{ GeV}^2$ is discovered in the upper half-plane for both $M_{\pi} \sim 210$ and 300 MeV , as shown in figure 2c. This pole suggests the existence of a possible virtual state and indicates that the strength of the attraction is too weak to form a bound state. However, the stability of this pole against ERE truncation remains unevaluated due to insufficient data for performing NLO fits.

5 Summary and outlook

We have presented the first lattice QCD study of S -wave interactions between doubly charmed baryons $B_{cc} \in \{\Xi_{cc}, \Omega_{cc}\}$ and Nambu-Goldstone bosons $\phi \in \{\pi, K\}$ at two pion masses $M_{\pi} \sim 210$ and 300 MeV using four $2 + 1$ flavor full-QCD ensembles provided by the CLQCD collaboration. Finite-volume energy levels for the four single channels, $\Omega_{cc}\bar{K}^{(-2,\frac{1}{2})}$, $\Xi_{cc}K^{(1,1)}$, $\Xi_{cc}K^{(1,0)}$ and $\Xi_{cc}\pi^{(0,\frac{3}{2})}$, are obtained. We find that the $\Xi_{cc}K^{(1,0)}$ channel is attractive due to negative energy shifts from the non-interacting thresholds, while the other channels are repulsive. It is worth noting that the same interacting information was also identified for the four single-channel $D\phi$ interactions in ref. [66], subject to the degeneracy between the $D\phi$ and $B_{cc}\phi$ systems under HDA symmetry. The phase shifts near thresholds are extracted by utilizing Lüscher's formula; consequently, the scattering lengths and effective ranges in the ERE are determined. Our results for the scattering lengths show robustness against the ERE truncation order and agree with previous

BChPT predictions after extrapolation to the physical point. Interestingly, pole analysis near the threshold implies a $J^P = 1/2^-$ virtual state in the $\Xi_{cc}K^{(1,0)}$ channel, located at $p^2 \approx -0.03$ GeV 2 . This work provides first-principle lattice-QCD inputs for theoretical investigations of double-heavy baryon spectroscopy, complementing ongoing experimental efforts. The present single-channel studies also pave the way for future exploration of the coupled-channel $B_{cc}\phi$ interactions.

Acknowledgments

We would like to thank Ying Chen, Feng-Kun Guo, Qu-Zhi Li, Chuan Liu, Peng Sun, Xiao-Nu Xiong and Yi-Bo Yang for helpful discussions. This work is supported by Science Research Project of Hebei Education Department under Contract No. QN2025063; National Nature Science Foundations of China (NSFC) under Contract Nos. 12275076, 11905258, 12335002, 12175279, 12293060, 12293061; by the Science Fund for Distinguished Young Scholars of Hunan Province under Grant No. 2024JJ2007; by Hebei Natural Science Foundation under Grant No. A2025205018; by the Science Foundation of Hebei Normal University with Contract No. L2025B09.

A Extraction of energies

In this section, we present the plots used to determine the masses of single hadrons and to illustrate the quality of the energy level fits for two-hadron systems. The effective masses for the π , K , Ξ_{cc} and Ω_{cc} are shown in figures 4, 5, 6 and 7, respectively. In these figures, the horizontal lines with bands indicate the fitted mass values and the corresponding temporal ranges used for the fits. For the two-hadron systems, figures 8, 9, 10 and 11 present the results from the two-exponential fits to the GEVP eigenvalues. To better visualize the fit quality, these figures plot the rescaled eigenvalues, which are expected to approach a constant at large time slices. The close agreement between the data points and the fit curves shown in the plots confirms the reliability of our extracted energy levels.

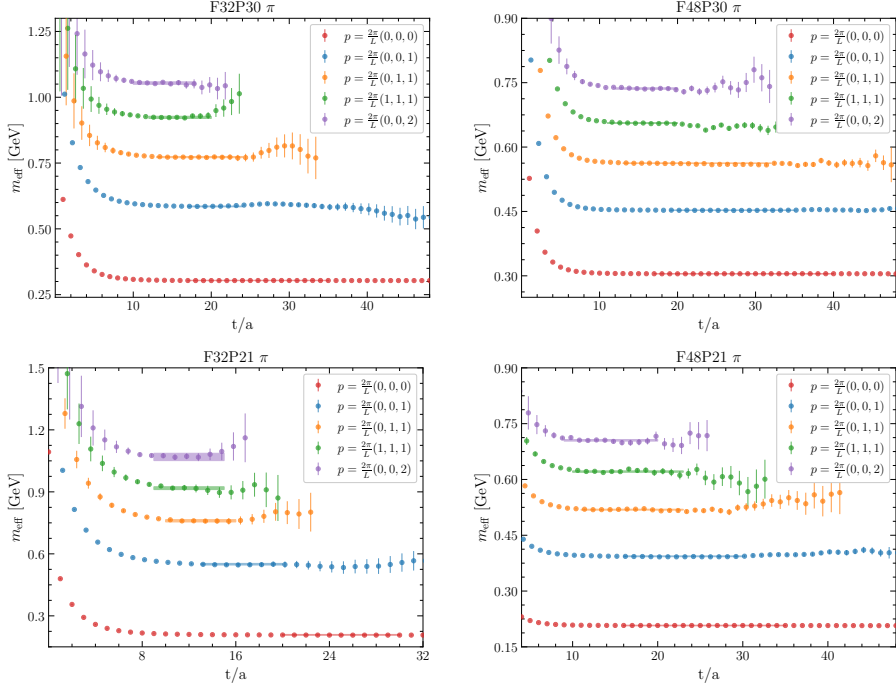


Figure 4: The pion effective mass plots for four ensembles. Each panel displays the results for the five lowest momenta, $\mathbf{p} = (0, 0, 0), (0, 0, 1), (0, 1, 1), (1, 1, 1),$ and $(0, 0, 2)$, in units of $2\pi/L$. The horizontal lines with bands indicate the fitted masses and the fitting ranges.

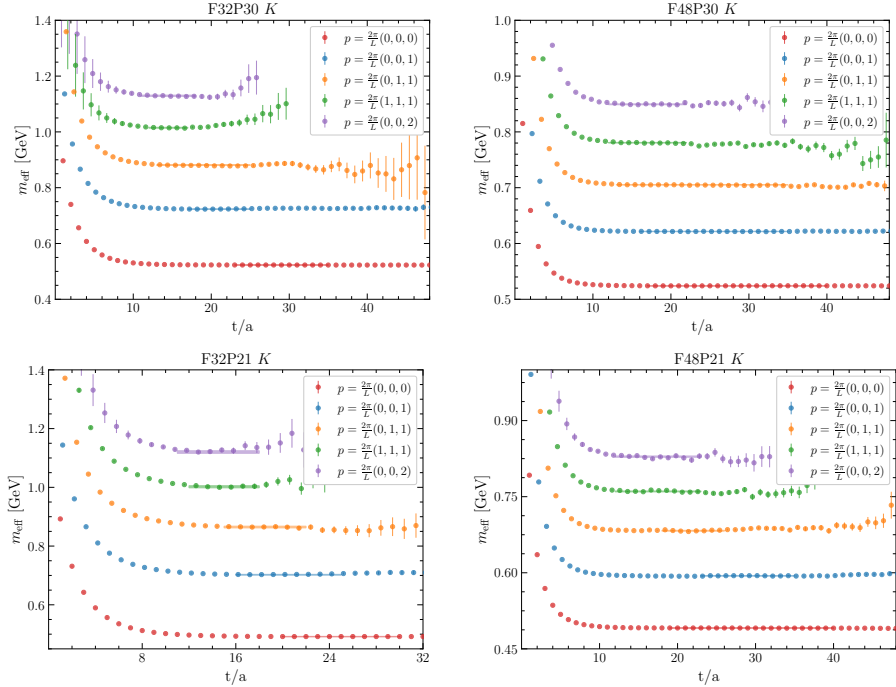


Figure 5: The kaon effective mass plots for four ensembles. The description is the same as in figure 4.

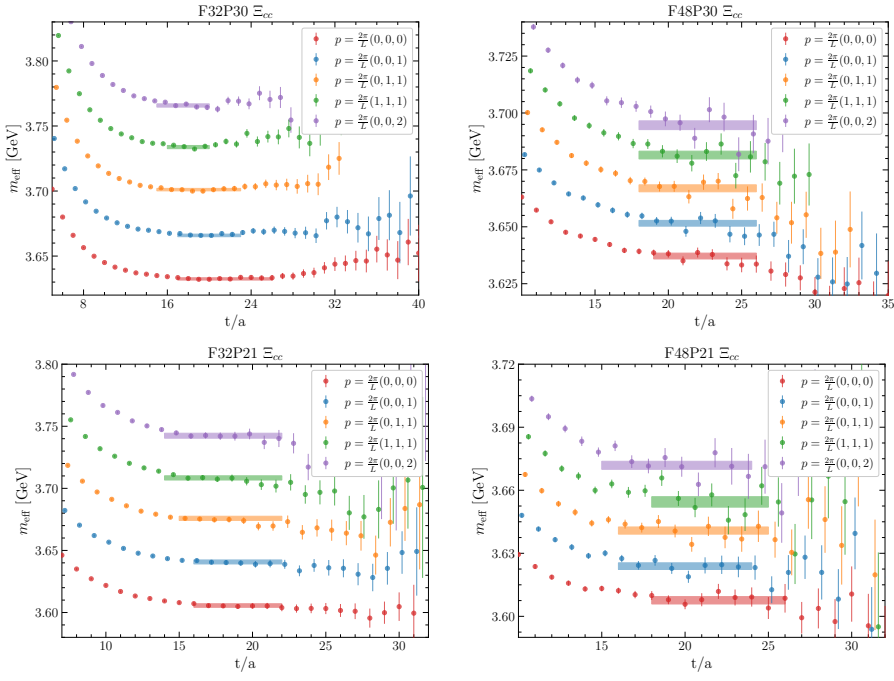


Figure 6: The Ξ_{cc} effective mass plots for four ensembles. The description is the same as in figure 4.

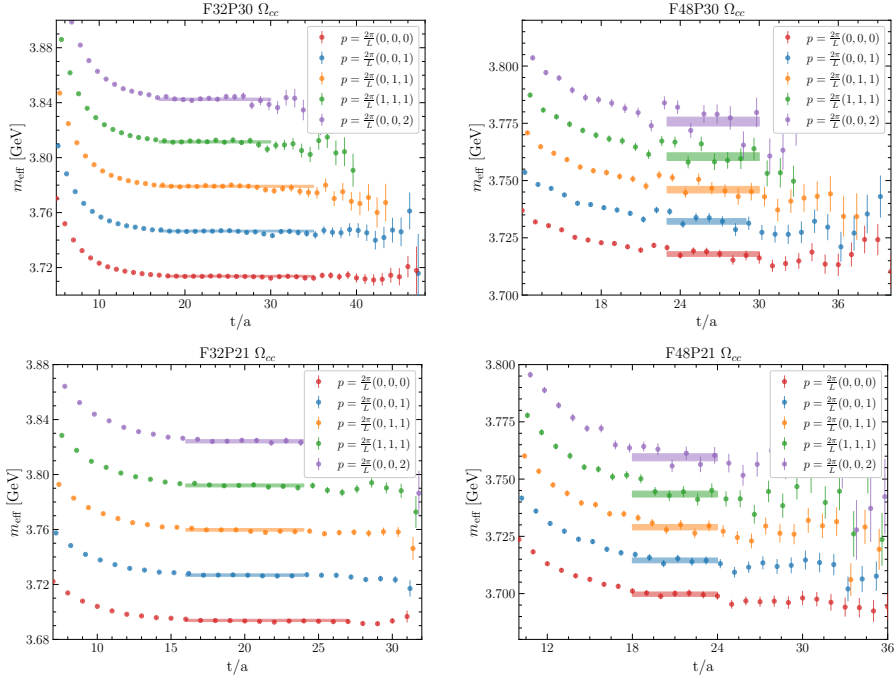


Figure 7: The Ω_{cc} effective mass plots for four ensembles. The description is the same as in figure 4.

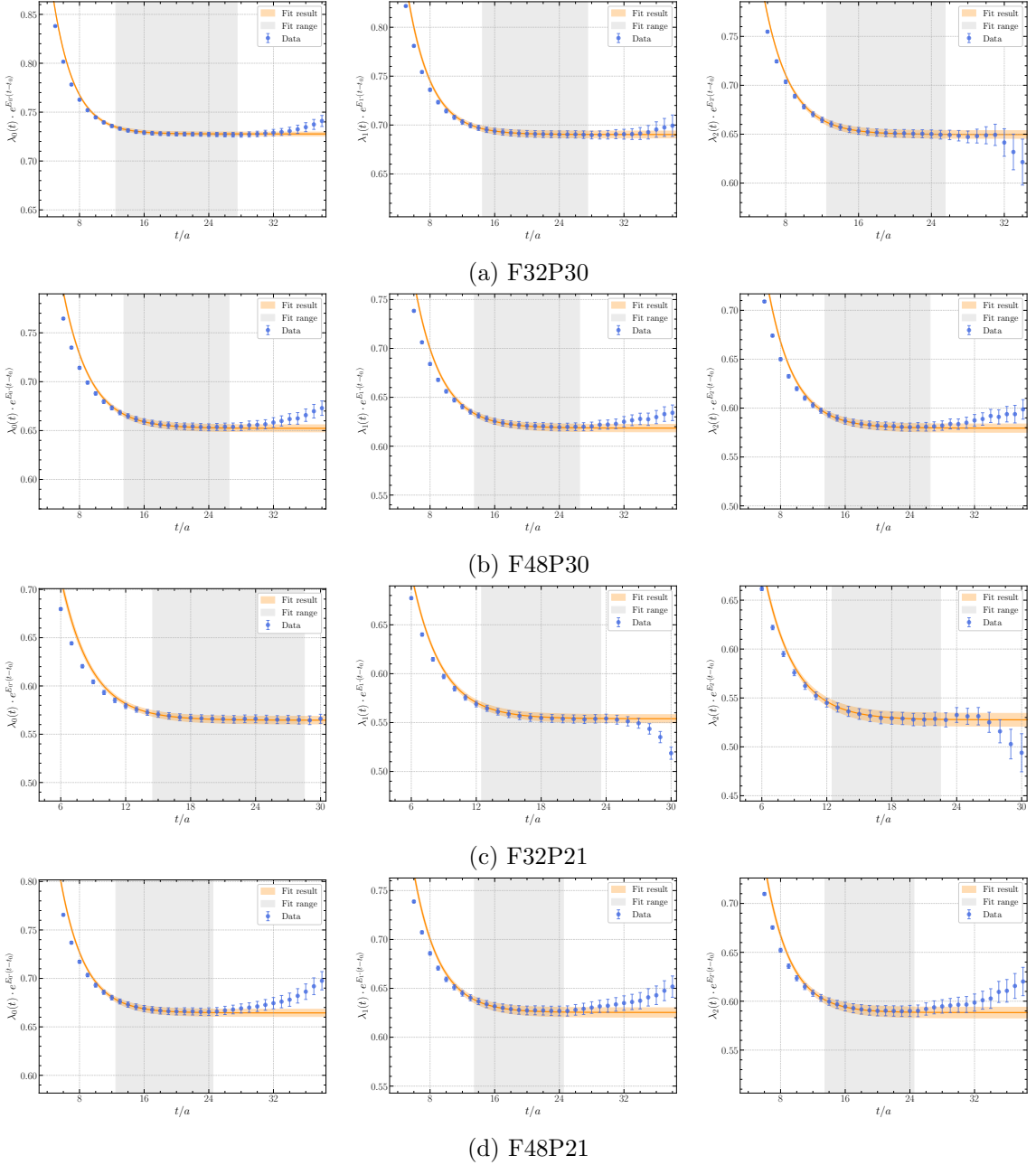


Figure 8: Fits of the GEVP eigenvalues λ_n for the $\Omega_{cc}\bar{K}^{(-2,1/2)}$ system. Plotted is the rescaled quantity $\lambda_n(t)e^{E_n(t-t_0)}$, which is expected to be constant at large time slices. The data points are shown in blue, while the yellow lines and bands represent the fit results with their statistical errors. The gray shaded areas indicate the temporal range used for the fits. Panels (a)-(d) show results on four different ensembles. Within each panel, the plots from left to right correspond to the three lowest momenta, corresponding to $|\mathbf{p}| = \{0, 1, \sqrt{2}\}$ (in units of $2\pi/L$).

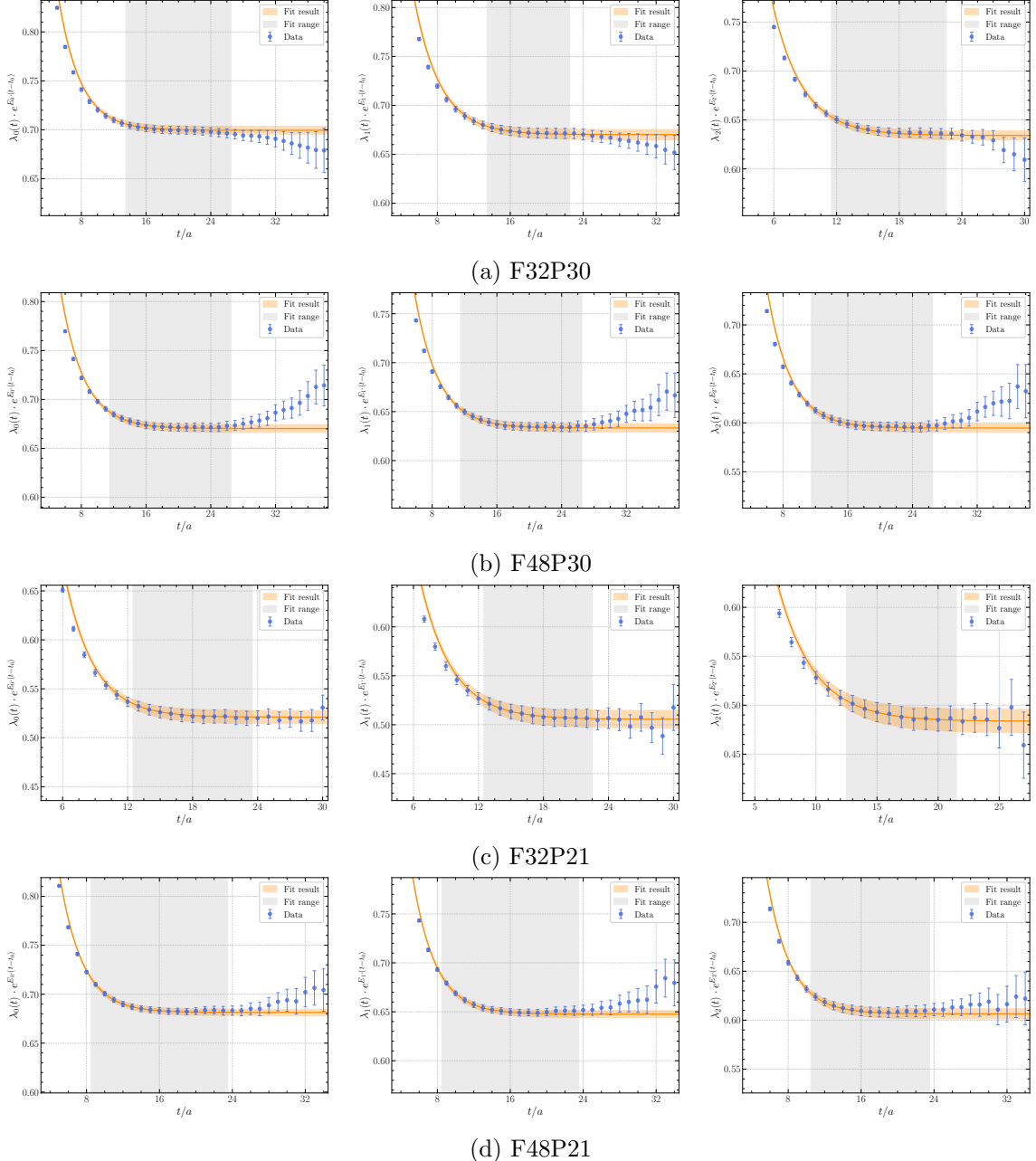


Figure 9: Fits of the GEVP eigenvalues λ_n for the $\Xi_{cc}K^{(1,0)}$ system on four ensembles. The description is the same as in figure 8.

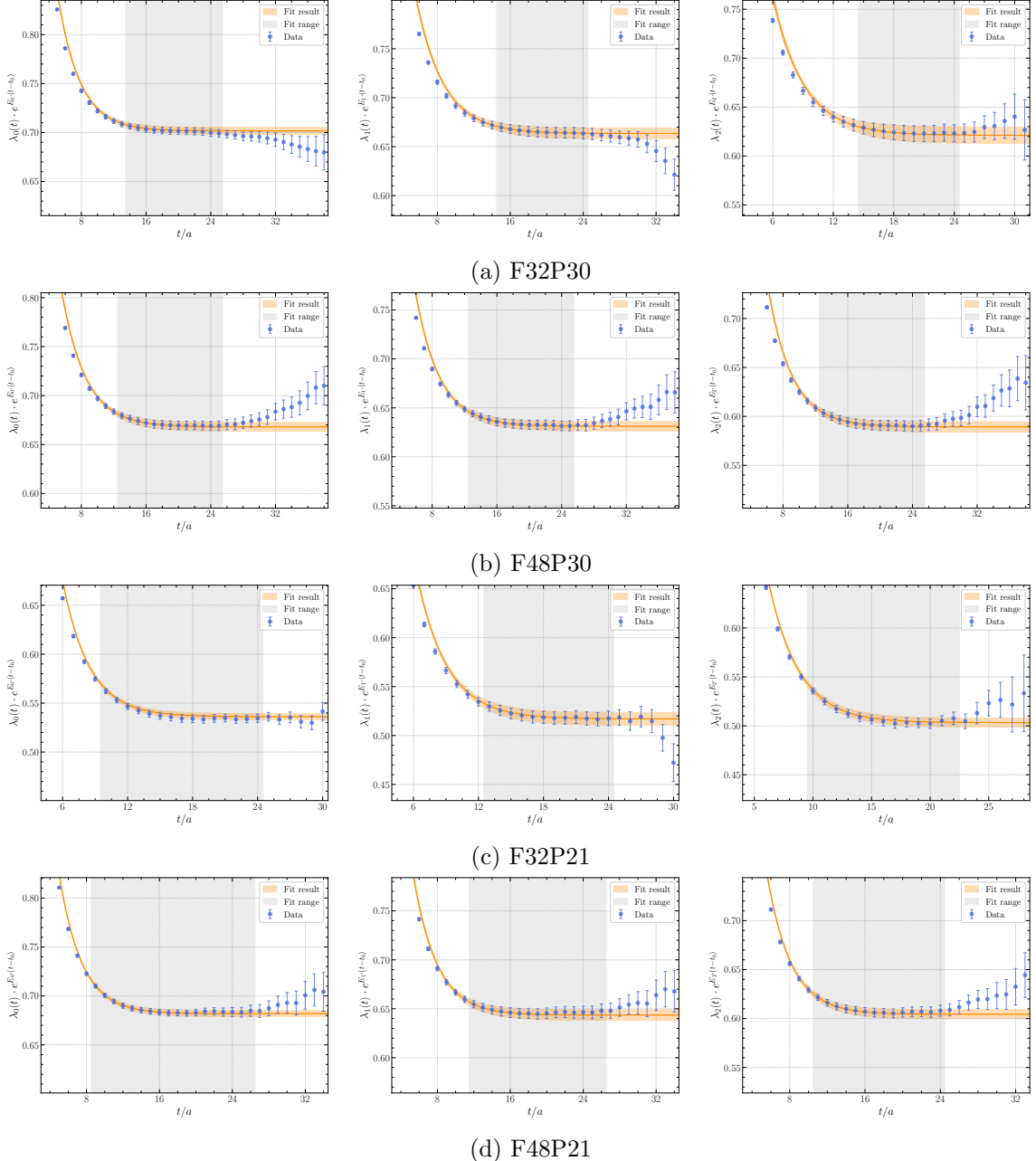


Figure 10: Fits of the GEVP eigenvalues λ_n for the $\Xi_{cc}K^{(1,1)}$ system on four ensembles. The description is the same as in figure 8.

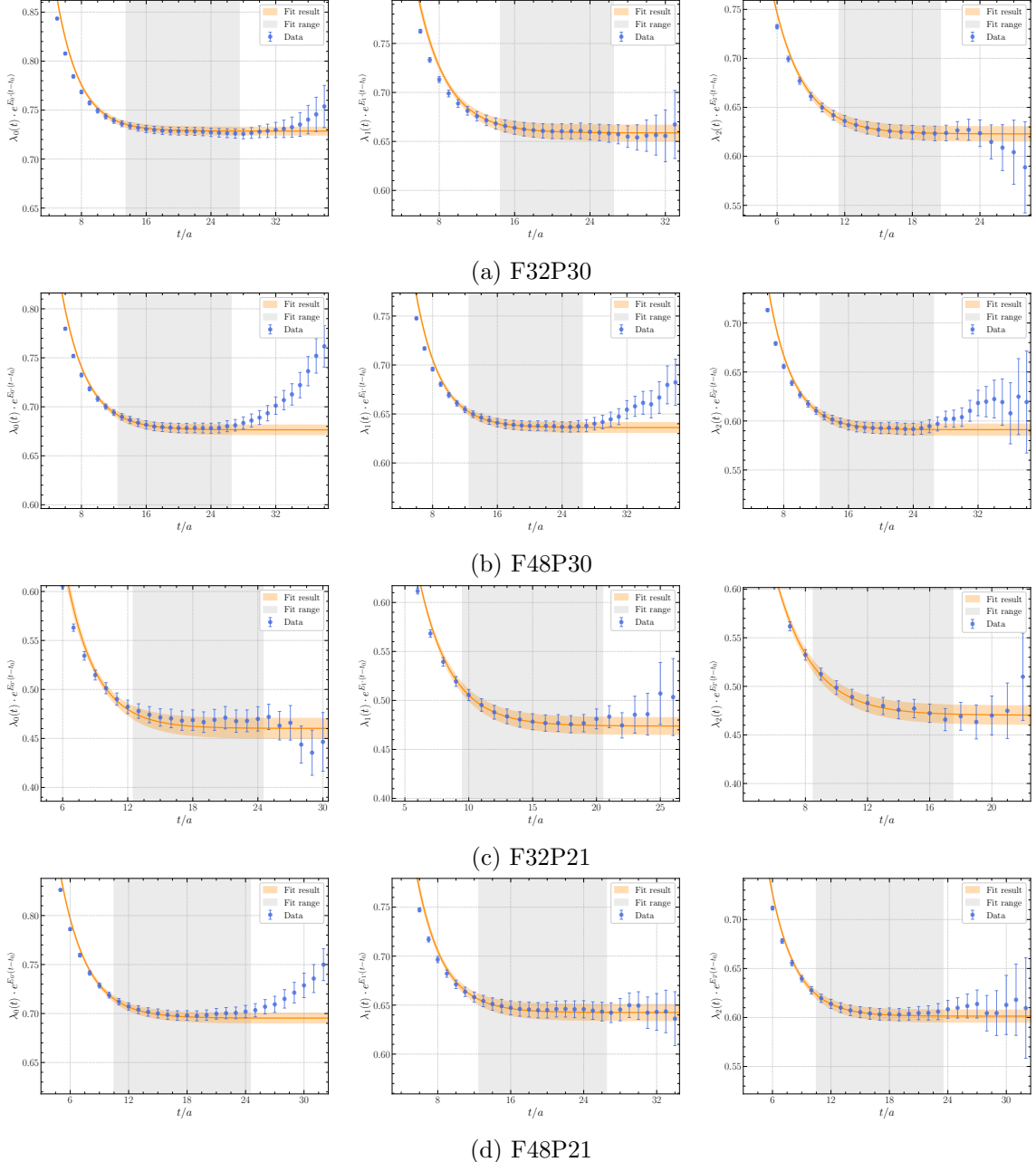


Figure 11: Fits of the GEVP eigenvalues λ_n for the $\Xi_{cc}\pi^{(0,3/2)}$ system on four ensembles. The description is the same as in figure 8.

B Influence of coupled-channel effects

As mentioned in section 3.3, we must consider some channels that may be encountered in our analysis of the two-particle system. The operators of D^+ , D^0 , D_s^+ , Λ_c^+ , Σ_c^{++} , and Ω_c^0 are needed, which are constructed as

$$\begin{aligned}
\mathcal{O}_{D^+}(x) &= \bar{d}(x)_\alpha^a (\gamma_5)_{\alpha\beta} c(x)_\beta^a, \\
\mathcal{O}_{D^0}(x) &= \bar{u}(x)_\alpha^a (\gamma_5)_{\alpha\beta} c(x)_\beta^a, \\
\mathcal{O}_{D_s^+}(x) &= \bar{s}(x)_\alpha^a (\gamma_5)_{\alpha\beta} c(x)_\beta^a, \\
\mathcal{O}_{\Lambda_c^+(udc)}(x) &= \epsilon^{ijk} P_+ [Q_u^{iT}(x) C \gamma_5 q_d^j(x)] Q_c^k(x), \\
\mathcal{O}_{\Sigma_c^{++}(uuc)}(x) &= \epsilon^{ijk} P_+ [Q_u^{iT}(x) C \gamma_5 q_c^j(x)] Q_u^k(x), \\
\mathcal{O}_{\Omega_c^0(ssc)}(x) &= \epsilon^{ijk} P_+ [Q_s^{iT}(x) C \gamma_5 q_c^j(x)] Q_s^k(x). \tag{B.1}
\end{aligned}$$

We perform simulations of the two-point correlation functions with the above interpolating fields. The corresponding masses are obtained and are listed in table 7. The influence of the $B_c D$ channels on our energy levels of $B_{cc}\phi$ systems is illustrated in figure 1, where $B_c \in \{\Sigma_c^{++}, \Omega_c^0, \Lambda_c^+\}$ and $D \in \{D^+, D^0, D_s^+\}$.

	D	D_s	Λ_c	Σ_c	Ω_c
F48P30	1.8923(4)	1.9706(2)	2.3488(9)	2.4943(19)	2.6703(11)
F48P21	1.8736(4)	1.9595(3)	2.2842(18)	2.4438(18)	2.6420(10)

Table 7: Masses of D , D_s , Λ_c , Σ_c , and Ω_c in units of GeV.

C Wick contractions

For completeness, we show the quark contraction diagrams for all four channels that are considered in our numerical computation in figures 12 to 15.

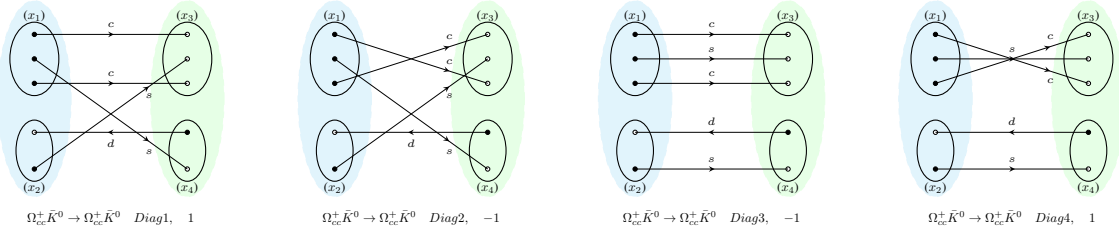


Figure 12: Sketch of the quark contraction for $\Omega_{cc}^+ \bar{K} \rightarrow \Omega_{cc}^+ \bar{K}$ with $(S, I) = (-2, 1/2)$.

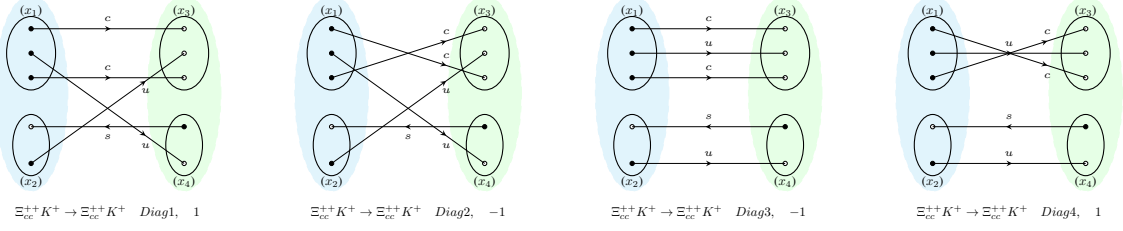


Figure 13: Sketch of the quark contraction for $\Xi_{cc}K \rightarrow \Xi_{cc}K$ with $(S, I) = (1, 1)$.

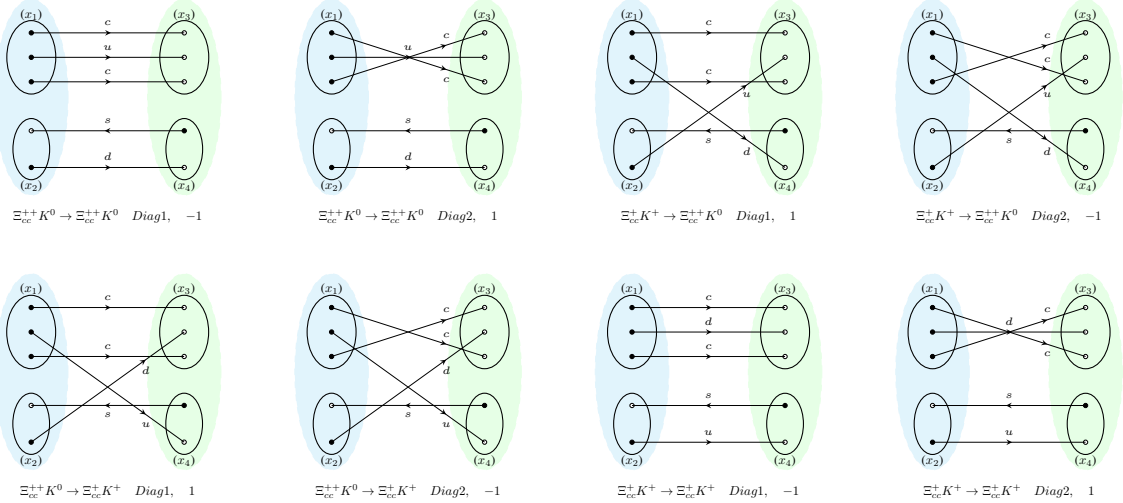


Figure 14: Sketch of the quark contraction for $\Xi_{cc}K \rightarrow \Xi_{cc}K$ with $(S, I) = (1, 0)$.

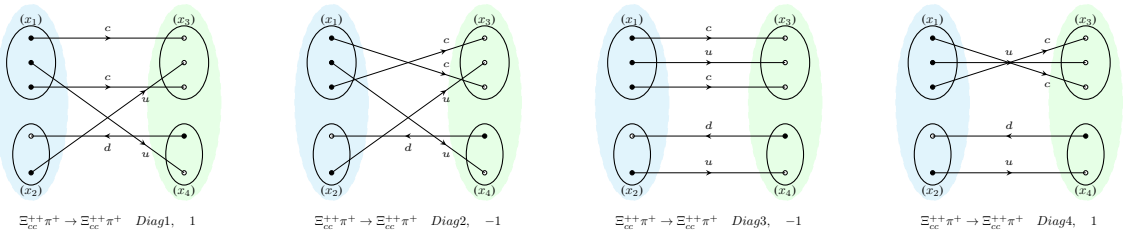


Figure 15: Sketch of the quark contraction for $\Xi_{cc}\pi \rightarrow \Xi_{cc}\pi$ with $(S, I) = (0, \frac{3}{2})$.

References

- [1] M. Gell-Mann, *A Schematic Model of Baryons and Mesons*, *Phys. Lett.* **8** (1964) 214.
- [2] PARTICLE DATA GROUP collaboration, *Review of particle physics*, *Phys. Rev. D* **110** (2024) 030001.
- [3] D.-L. Yao, L.-Y. Dai, H.-Q. Zheng and Z.-Y. Zhou, *A review on partial-wave dynamics with chiral effective field theory and dispersion relation*, *Rept. Prog. Phys.* **84** (2021) 076201 [[2009.13495](#)].
- [4] H.-Y. Cheng, *Charmed baryon physics circa 2021*, *Chin. J. Phys.* **78** (2022) 324 [[2109.01216](#)].
- [5] L. Meng, B. Wang, G.-J. Wang and S.-L. Zhu, *Chiral perturbation theory for heavy hadrons and chiral effective field theory for heavy hadronic molecules*, *Phys. Rept.* **1019** (2023) 1 [[2204.08716](#)].
- [6] H.-X. Chen, W. Chen, X. Liu, Y.-R. Liu and S.-L. Zhu, *An updated review of the new hadron states*, *Rept. Prog. Phys.* **86** (2023) 026201 [[2204.02649](#)].
- [7] V. Crede and J. Yelton, *70 years of hyperon spectroscopy: a review of strange Ξ , Ω baryons, and the spectrum of charmed and bottom baryons*, *Rept. Prog. Phys.* **87** (2024) 106301 [[2502.08815](#)].
- [8] LHCb collaboration, *Observation of the doubly charmed baryon Ξ_{cc}^{++}* , *Phys. Rev. Lett.* **119** (2017) 112001 [[1707.01621](#)].
- [9] F.-S. Yu, H.-Y. Jiang, R.-H. Li, C.-D. Lü, W. Wang and Z.-X. Zhao, *Discovery Potentials of Doubly Charmed Baryons*, *Chin. Phys. C* **42** (2018) 051001 [[1703.09086](#)].
- [10] LHCb collaboration, *First Observation of the Doubly Charmed Baryon Decay $\Xi_{cc}^{++} \rightarrow \Xi_c^+ \pi^+$* , *Phys. Rev. Lett.* **121** (2018) 162002 [[1807.01919](#)].
- [11] LHCb collaboration, *Observation of the doubly charmed baryon decay $\Xi_{cc}^{++} \rightarrow \Xi_c' \pi^+$* , *JHEP* **05** (2022) 038 [[2202.05648](#)].
- [12] LHCb collaboration, *Observation of the doubly-charmed-baryon decay $\Xi_{cc}^{++} \rightarrow \Xi_c^0 \pi^+ \pi^+$* , [2504.05063](#).
- [13] LHCb collaboration, *Precision measurement of the Ξ_{cc}^{++} mass*, *JHEP* **02** (2020) 049 [[1911.08594](#)].
- [14] LHCb collaboration, *Measurement of the Lifetime of the Doubly Charmed Baryon Ξ_{cc}^{++}* , *Phys. Rev. Lett.* **121** (2018) 052002 [[1806.02744](#)].
- [15] LHCb collaboration, *Measurement of Ξ_{cc}^{++} production in pp collisions at $\sqrt{s} = 13$ TeV*, *Chin. Phys. C* **44** (2020) 022001 [[1910.11316](#)].
- [16] D. Ebert, R.N. Faustov, V.O. Galkin and A.P. Martynenko, *Mass spectra of doubly heavy baryons in the relativistic quark model*, *Phys. Rev. D* **66** (2002) 014008 [[hep-ph/0201217](#)].
- [17] W. Roberts and M. Pervin, *Heavy baryons in a quark model*, *Int. J. Mod. Phys. A* **23** (2008) 2817 [[0711.2492](#)].
- [18] V.V. Kiselev and A.K. Likhoded, *Baryons with two heavy quarks*, *Phys. Usp.* **45** (2002) 455 [[hep-ph/0103169](#)].
- [19] J.-R. Zhang and M.-Q. Huang, *Doubly heavy baryons in QCD sum rules*, *Phys. Rev. D* **78** (2008) 094007 [[0810.5396](#)].

- [20] Z.-G. Wang, *Analysis of the $\frac{1}{2}^+$ doubly heavy baryon states with QCD sum rules*, *Eur. Phys. J. A* **45** (2010) 267 [[1001.4693](#)].
- [21] R. Lewis, N. Mathur and R.M. Woloshyn, *Charmed baryons in lattice QCD*, *Phys. Rev. D* **64** (2001) 094509 [[hep-ph/0107037](#)].
- [22] UKQCD collaboration, *Spectroscopy of doubly charmed baryons in lattice QCD*, *JHEP* **07** (2003) 066 [[hep-lat/0307025](#)].
- [23] L. Liu, H.-W. Lin, K. Orginos and A. Walker-Loud, *Singly and Doubly Charmed $J=1/2$ Baryon Spectrum from Lattice QCD*, *Phys. Rev. D* **81** (2010) 094505 [[0909.3294](#)].
- [24] SELEX collaboration, *First Observation of the Doubly Charmed Baryon Ξ_{cc}^+* , *Phys. Rev. Lett.* **89** (2002) 112001 [[hep-ex/0208014](#)].
- [25] SELEX collaboration, *Confirmation of the Double Charm Baryon $\Xi_{cc}^+(3520)$ via its Decay to pD^+K^-* , *Phys. Lett. B* **628** (2005) 18 [[hep-ex/0406033](#)].
- [26] S.P. Ratti, *New Results on C-Baryons and a Search for CC-Baryons in FOCUS*, *Nucl. Phys. B Proc. Suppl.* **115** (2003) 33.
- [27] BABAR collaboration, *Search for doubly charmed baryons Ξ_{cc}^+ and Ξ_{cc}^{++} in BABAR*, *Phys. Rev. D* **74** (2006) 011103 [[hep-ex/0605075](#)].
- [28] BELLE collaboration, *Observation of new states decaying into $\Lambda_c^+K^-\pi^+$ and $\Lambda_c^+K_S^0\pi^-$* , *Phys. Rev. Lett.* **97** (2006) 162001 [[hep-ex/0606051](#)].
- [29] LHCb collaboration, *Search for the doubly charmed baryon Ξ_{cc}^+* , *JHEP* **12** (2013) 090 [[1310.2538](#)].
- [30] LHCb collaboration, *Search for the doubly charmed baryon Ξ_{cc}^+* , *Sci. China Phys. Mech. Astron.* **63** (2020) 221062 [[1909.12273](#)].
- [31] D.-L. Yao, *Masses and sigma terms of doubly charmed baryons up to $\mathcal{O}(p^4)$ in manifestly Lorentz-invariant baryon chiral perturbation theory*, *Phys. Rev. D* **97** (2018) 034012 [[1801.09462](#)].
- [32] E. Ortiz-Pacheco and R. Bijker, *Masses and radiative decay widths of S- and P-wave singly, doubly, and triply heavy charm and bottom baryons*, *Phys. Rev. D* **108** (2023) 054014 [[2307.04939](#)].
- [33] Z.-Y. Li, G.-L. Yu, Z.-G. Wang, J.-Z. Gu and H.-T. Shen, *Mass spectra of doubly heavy baryons in the relativized quark model with heavy-quark dominance*, [2506.19504](#).
- [34] LHCb collaboration, *Search for the doubly charmed baryon Ω_{cc}^+* , *Sci. China Phys. Mech. Astron.* **64** (2021) 101062 [[2105.06841](#)].
- [35] LHCb collaboration, *Search for the doubly charmed baryon Ξ_{cc}^+ in the $\Xi_c^+\pi^-\pi^+$ final state*, *JHEP* **12** (2021) 107 [[2109.07292](#)].
- [36] H. Na and S.A. Gottlieb, *Charm and bottom heavy baryon mass spectrum from lattice QCD with 2+1 flavors*, *PoS LATTICE2007* (2007) 124 [[0710.1422](#)].
- [37] H. Na and S. Gottlieb, *Heavy baryon mass spectrum from lattice QCD with 2+1 dynamical sea quark flavors*, *PoS LATTICE2008* (2008) 119 [[0812.1235](#)].
- [38] S. Basak, S. Datta, M. Padmanath, P. Majumdar and N. Mathur, *Charm and strange hadron spectra from overlap fermions on HISQ gauge configurations*, *PoS LATTICE2012* (2012) 141 [[1211.6277](#)].

- [39] R.A. Briceno, H.-W. Lin and D.R. Bolton, *Charmed-Baryon Spectroscopy from Lattice QCD with $N_f = 2+1+1$ Flavors*, *Phys. Rev. D* **86** (2012) 094504 [[1207.3536](#)].
- [40] S. Durr, G. Koutsou and T. Lippert, *Meson and Baryon dispersion relations with Brillouin fermions*, *Phys. Rev. D* **86** (2012) 114514 [[1208.6270](#)].
- [41] PACS-CS collaboration, *Charmed baryons at the physical point in 2+1 flavor lattice QCD*, *Phys. Rev. D* **87** (2013) 094512 [[1301.4743](#)].
- [42] Z.S. Brown, W. Detmold, S. Meinel and K. Orginos, *Charmed bottom baryon spectroscopy from lattice QCD*, *Phys. Rev. D* **90** (2014) 094507 [[1409.0497](#)].
- [43] M. Padmanath, R.G. Edwards, N. Mathur and M. Peardon, *Spectroscopy of doubly-charmed baryons from lattice QCD*, *Phys. Rev. D* **91** (2015) 094502 [[1502.01845](#)].
- [44] P. Pérez-Rubio, S. Collins and G.S. Bali, *Charmed baryon spectroscopy and light flavor symmetry from lattice QCD*, *Phys. Rev. D* **92** (2015) 034504 [[1503.08440](#)].
- [45] C. Alexandrou and C. Kallidonis, *Low-lying baryon masses using $N_f = 2$ twisted mass clover-improved fermions directly at the physical pion mass*, *Phys. Rev. D* **96** (2017) 034511 [[1704.02647](#)].
- [46] N. Mathur and M. Padmanath, *Lattice QCD study of doubly-charmed strange baryons*, *Phys. Rev. D* **99** (2019) 031501 [[1807.00174](#)].
- [47] H. Bahtiyar, K.U. Can, G. Erkol, P. Gubler, M. Oka and T.T. Takahashi, *Charmed baryon spectrum from lattice QCD near the physical point*, *Phys. Rev. D* **102** (2020) 054513 [[2004.08999](#)].
- [48] C. Alexandrou, S. Bacchio, G. Christou and J. Finkenrath, *Low-lying baryon masses using twisted mass fermions ensembles at the physical pion mass*, *Phys. Rev. D* **108** (2023) 094510 [[2309.04401](#)].
- [49] K.U. Can, G. Erkol, B. Isildak, M. Oka and T.T. Takahashi, *Electromagnetic properties of doubly charmed baryons in Lattice QCD*, *Phys. Lett. B* **726** (2013) 703 [[1306.0731](#)].
- [50] K.U. Can, G. Erkol, B. Isildak, M. Oka and T.T. Takahashi, *Electromagnetic structure of charmed baryons in Lattice QCD*, *JHEP* **05** (2014) 125 [[1310.5915](#)].
- [51] K.U. Can, *Lattice QCD study of the elastic and transition form factors of charmed baryons*, *Int. J. Mod. Phys. A* **36** (2021) 2130013 [[2107.13159](#)].
- [52] H. Bahtiyar, *Electromagnetic structure of spin- $\frac{1}{2}$ doubly charmed baryons in lattice QCD*, *Phys. Rev. D* **108** (2023) 034504 [[2209.05361](#)].
- [53] H. Bahtiyar, K.U. Can, G. Erkol, M. Oka and T.T. Takahashi, *Radiative transitions of doubly charmed baryons in lattice QCD*, *Phys. Rev. D* **98** (2018) 114505 [[1807.06795](#)].
- [54] G. Aarts, C. Allton, M.N. Anwar, R. Bignell, T.J. Burns, B. Jäger et al., *Non-zero temperature study of spin 1/2 charmed baryons using lattice gauge theory*, *Eur. Phys. J. A* **60** (2024) 59 [[2308.12207](#)].
- [55] J. Gasser and H. Leutwyler, *Chiral Perturbation Theory to One Loop*, *Annals Phys.* **158** (1984) 142.
- [56] J. Gasser and H. Leutwyler, *Chiral Perturbation Theory: Expansions in the Mass of the Strange Quark*, *Nucl. Phys. B* **250** (1985) 465.
- [57] J. Gasser, M.E. Sainio and A. Svarc, *Nucleons with chiral loops*, *Nucl. Phys. B* **307** (1988) 779.

- [58] S. Weinberg, *Phenomenological Lagrangians*, *Physica A* **96** (1979) 327.
- [59] L. Meng and S.-L. Zhu, *Light pseudoscalar meson and doubly charmed baryon scattering lengths with heavy diquark-antiquark symmetry*, *Phys. Rev. D* **100** (2019) 014006 [[1811.07320](#)].
- [60] Z.-R. Liang, P.-C. Qiu and D.-L. Yao, *One-loop analysis of the interactions between doubly charmed baryons and Nambu-Goldstone bosons*, *JHEP* **07** (2023) 124 [[2303.03370](#)].
- [61] T. Fuchs, J. Gegelia, G. Japaridze and S. Scherer, *Renormalization of relativistic baryon chiral perturbation theory and power counting*, *Phys. Rev. D* **68** (2003) 056005 [[hep-ph/0302117](#)].
- [62] Z.-H. Guo, *Prediction of exotic doubly charmed baryons within chiral effective field theory*, *Phys. Rev. D* **96** (2017) 074004 [[1708.04145](#)].
- [63] M.-J. Yan, X.-H. Liu, S. González-Solís, F.-K. Guo, C. Hanhart, U.-G. Meißner et al., *New spectrum of negative-parity doubly charmed baryons: Possibility of two quasistable states*, *Phys. Rev. D* **98** (2018) 091502 [[1805.10972](#)].
- [64] P.-C. Qiu and D.-L. Yao, *Chiral effective Lagrangian for doubly charmed baryons up to $\mathcal{O}(q^4)$* , *Phys. Rev. D* **103** (2021) 034006 [[2012.11117](#)].
- [65] H. Liu, Y.-H. Zou, Y.-R. Liu and S.-Z. Jiang, *Chiral Lagrangians for spin- $\frac{1}{2}$ and spin- $\frac{3}{2}$ doubly charmed baryons*, *Phys. Rev. D* **108** (2023) 014032 [[2304.04575](#)].
- [66] L. Liu, K. Orginos, F.-K. Guo, C. Hanhart and U.-G. Meißner, *Interactions of charmed mesons with light pseudoscalar mesons from lattice QCD and implications on the nature of the $D_{s0}^*(2317)$* , *Phys. Rev. D* **87** (2013) 014508 [[1208.4535](#)].
- [67] D.-L. Yao, M.-L. Du, F.-K. Guo and U.-G. Meißner, *One-loop analysis of the interactions between charmed mesons and Goldstone bosons*, *JHEP* **11** (2015) 058 [[1502.05981](#)].
- [68] M.J. Savage and M.B. Wise, *Spectrum of baryons with two heavy quarks*, *Phys. Lett. B* **248** (1990) 177.
- [69] CLQCD collaboration, *Quark masses and low-energy constants in the continuum from the tadpole-improved clover ensembles*, *Phys. Rev. D* **109** (2024) 054507 [[2310.00814](#)].
- [70] S. Prelovsek, U. Skerbis and C.B. Lang, *Lattice operators for scattering of particles with spin*, *JHEP* **01** (2017) 129 [[1607.06738](#)].
- [71] M. Lüscher, *Two particle states on a torus and their relation to the scattering matrix*, *Nucl. Phys. B* **354** (1991) 531.
- [72] M. Lüscher, *Signatures of unstable particles in finite volume*, *Nucl. Phys. B* **364** (1991) 237.
- [73] A.X. El-Khadra, A.S. Kronfeld and P.B. Mackenzie, *Massive fermions in lattice gauge theory*, *Phys. Rev. D* **55** (1997) 3933 [[hep-lat/9604004](#)].
- [74] HADRON SPECTRUM collaboration, *A Novel quark-field creation operator construction for hadronic physics in lattice QCD*, *Phys. Rev. D* **80** (2009) 054506 [[0905.2160](#)].
- [75] E. Berkowitz, T. Kurth, A. Nicholson, B. Joo, E. Rinaldi, M. Strother et al., *Two-Nucleon Higher Partial-Wave Scattering from Lattice QCD*, *Phys. Lett. B* **765** (2017) 285 [[1508.00886](#)].
- [76] S.J. Wallace, *Partial-wave and helicity operators for the scattering of two hadrons in lattice QCD*, *Phys. Rev. D* **92** (2015) 034520 [[1506.05492](#)].

- [77] M. Gockeler, R. Horsley, M. Lage, U.G. Meissner, P.E.L. Rakow, A. Rusetsky et al., *Scattering phases for meson and baryon resonances on general moving-frame lattices*, *Phys. Rev. D* **86** (2012) 094513 [[1206.4141](#)].
- [78] J.J. Dudek, R.G. Edwards and C.E. Thomas, *S and D-wave phase shifts in isospin-2 $\pi\pi$ scattering from lattice QCD*, *Phys. Rev. D* **86** (2012) 034031 [[1203.6041](#)].
- [79] M. Lüscher and U. Wolff, *How to Calculate the Elastic Scattering Matrix in Two-dimensional Quantum Field Theories by Numerical Simulation*, *Nucl. Phys. B* **339** (1990) 222.
- [80] B. Blossier, M. Della Morte, G. von Hippel, T. Mendes and R. Sommer, *On the generalized eigenvalue method for energies and matrix elements in lattice field theory*, *JHEP* **04** (2009) 094 [[0902.1265](#)].
- [81] R.A. Briceno, *Two-particle multichannel systems in a finite volume with arbitrary spin*, *Phys. Rev. D* **89** (2014) 074507 [[1401.3312](#)].
- [82] M. Padmanath and S. Prelovsek, *Signature of a Doubly Charm Tetraquark Pole in DD^* Scattering on the Lattice*, *Phys. Rev. Lett.* **129** (2022) 032002 [[2202.10110](#)].
- [83] S. Prelovsek, S. Collins, D. Mohler, M. Padmanath and S. Piemonte, *Charmonium-like resonances with $J^{PC} = 0^{++}, 2^{++}$ in coupled $D\bar{D}$, $D_s\bar{D}_s$ scattering on the lattice*, *JHEP* **06** (2021) 035 [[2011.02542](#)].
- [84] S. Piemonte, S. Collins, D. Mohler, M. Padmanath and S. Prelovsek, *Charmonium resonances with $J^{PC} = 1^{--}$ and 3^{--} from $\bar{D}D$ scattering on the lattice*, *Phys. Rev. D* **100** (2019) 074505 [[1905.03506](#)].
- [85] H. Xing, J. Liang, L. Liu, P. Sun and Y.-B. Yang, *First observation of the hidden-charm pentaquarks on lattice*, [2210.08555](#).